Eur. Phys. J. Special Topics **208**, 189–216 (2012)

DOI: 10.1140/epjst/e2012-01619-x

THE EUROPEAN PHYSICAL JOURNAL SPECIAL TOPICS

Review

Multiwavelength anomalous diffraction and diffraction anomalous fine structure to study composition and strain of semiconductor nanostructures

MAD and DAFS for studying Semiconductor Nanostructures

V. Favre-Nicolin[1], M.G. Proietti[2], C. Leclere[3], N.A. Katcho[4,2], M.-I. Richard[5], and H. Renevier[3,a]

[1] CEA-UJF, INAC, SP2M, Grenoble, France
[2] ICMA, Dep. Fisica de la Materia Condensada, CSIC-Universidad de Zaragoza, Spain
[3] LMGP, Grenoble INP - Minatec, Grenoble, France
[4] IQFR-CSIC, Madrid, Spain
[5] Aix-Marseille Université, IM2NP-CNRS, Faculté des Sciences et Techniques, 13397 Marseille Cedex, France

Received 15 December 2011 / Received in final form 23 March 2012
Published online 15 June 2012

Abstract. The aim of this paper is to illustrate the use of Multi-Wavelength Anomalous Diffraction (MAD) and Diffraction Anomalous Fine Structure (DAFS) spectroscopy for the study of structural properties of semiconductor nanostructures. We give a brief introduction on the basic principles of these techniques providing a detailed bibliography. Then we focus on the data reduction and analysis and we give specific examples of their application on three different kinds of semiconductor nanostructures: Ge/Si nanoislands, AlN capped GaN/AlN Quantum Dots and AlGaN/AlN Nanowires. We show that the combination of MAD and DAFS is a very powerful tool to solve the structural problem of these materials of high technological impact. In particular, the effects of composition and strain on diffraction are disentangled and composition can be determined in a reliable way, even at the interface between nanostructure and substrate. We show the great possibilities of this method and give the reader the basic tools to undertake its use.

1 Introduction

Multiwavelength Anomalous Diffraction (MAD) was first developed in the 1980's in order to solve macromolecular structures [1–3]. The principle was to enhance the scattering from selected (resonant) atoms by changing the incident photon energy around

[a] e-mail: hubert.renevier@grenoble-inp.fr

one of their absorption edges, and experimentally solving the crystallographic phase problem. Similarly to X-ray Absorption Fine Structure (XAFS) spectroscopy, Diffraction Anomalous Fine Structure (DAFS) spectroscopy provides information about the empty electronic orbitals/states and the local atomic environment of resonant (anomalous) atoms selected by the diffraction condition [4–7]. The appearance of Diffraction Anomalous Fine Structure (DAFS) in the diffracted intensity was observed for the first time in the mid-fifties by Y. Cauchois [8,9]. Since then, applications/studies have been sporadic [10–12], until Stragier et al. [4] gave an elegant demonstration of the interest of DAFS with a Cu single cristal. Soon after I.J. Pickering et al. [13,14] measured DAFS spectra of powdered magnetite. The reader can find extensive information about the early days of DAFS in the review articles by Sorensen et al. [15] and more recently by Hodeau et al. [3].

The very long incubation of DAFS could seem quite surprising if one thinks of the vast and massive application of Extended XAFS and X-ray Diffraction (XRD) to material science in the last thirty years. Indeed, DAFS provides both the advantages of X-ray diffraction and absorption, but it is more than addition of absorption and diffraction, it is simultaneously a *site* and *chemically* selective probe. For instance, in case of samples in which different local environments coexist, XAFS spectroscopy may fail to give pertinent information since, due to the lack of spatial selectivity, all the different environments are probed. The site/spatial selectivity of DAFS helps to solve the difficulty by selecting individual sites, which is clearly interesting for both absorption and diffraction scientific communities.

One of the reasons why this technique did not take off rapidly is that, from a technical point of view, it presents tight experimental requirements. Essentially one needs an undistorted signal and a very high signal-to-noise ratio as a function of the energy, as for Extended XAFS (EXAFS), to perform a quantitative analysis of fine structure oscillations, an analysis on a diffraction yield that is only a very small fraction of the total one (usually few %). Fortunately, the development of Synchrotron Radiation facilities, including third generation sources, has marked an advance for a number of new spectroscopic techniques, among them DAFS.

Together with technical improvements, data analysis has also come along, relying on one hand on the solid support and established MAD data treatment, and, on the other hand, on the EXAFS approach [4,12], using available and well-known codes for *ab initio* calculations, data simulation and analysis. Indeed, although DAFS contains contributions of both the real and imaginary parts of the complex anomalous scattering factors (XAFS is proportional to the imaginary part), they can be analyzed, in the extended region, like EXAFS [16]. An efficient program for simulating the near edge DAFS is now also available [17].

However, one must mention an intrinsic limitation of DAFS that is the difficulty (but it is not always impossible!) to correct the data for self absorption when measuring bulk samples (see for instance [18,19]). Therefore the method is definitely well suited for studying thin films or heterostructures [5,20–25]. Also, in some cases, multiple diffraction inside the sample can be a source of signal distorsion.

In the past few years MAD and DAFS have been applied to systems of great technological interest as semiconductor nanostructures [26–30]. The knowledge of strain, chemical composition, inter-mixing at the interfaces – i.e. structural properties at the long and short range scale - are of great importance to understand the growth mechanism as well as the electronic and optical properties of hetero and nanostructures. Strain is closely related to composition, shape and aspect ratio of the nanostructures, and on the mutual stress which nanostructures, substrate and the matrix apply to each other.

X-ray diffraction is known to be a powerful tool for measuring strain fields (see ref. [31,32]). The combination of MAD (see Sect. 2), which allows to extract the

scattering amplitudes of resonant and non resonant atoms (chemical mapping in reciprocal space), and DAFS, which allows to determine the local environment of atoms located in an iso-strain volume [33] selected by diffraction is a very powerful approach to disentangle strain and compostion.

In addition, X-ray diffraction is a non destructive method that averages over many individual nanostructure and gives statistically relevant structural properties such as strain and composition. However, the structural properties of individual nanostructures can be obtained by using sub-micron beam size and/or coherent scattering (see for instance [34]).

A major technical improvement of DAFS spectroscopy, that is thoroughly described in this article, is to perform the experiment in grazing incidence geometry (GIMAD and GIDAFS) to reduce the substrate scattering contribution, allowing to focus on the structural properties of nanoobjects [35,36]. The examples that we give of GIDAFS applications refer indeed to challenging nano-materials with strong technological impact.

2 Multiwavelength anomalous diffraction and grazing incidence MAD: Principles

The atomic scattering factor can be written as:

$$f(\mathbf{Q}, E) = f^0(Q) + f'(E) + if''(E) \tag{1}$$

where $\mathbf{Q}$ is the scattering vector, Q its amplitude, E the photon energy, f^0 the Thomson atomic scattering factor, f' (respectively f'') the real (resp. imaginary) parts of the resonant scattering factor. When performing a MAD experiment, f' and f'' can be measured before the diffraction experiment, generally using a fluorescence measurement [3]. As is shown in Fig. 1, f' and f'' depend both on the environment of the resonant atom and on the polarization of the incoming X-ray beam: this anisotropy of anomalous scattering [37–40] must be taken into account when analysing diffraction data.

To calculate the diffracted intensity, let us consider an assembly of N atoms comprising N_A resonant (anomalous) atoms A. The structure factor is

$$F = \sum_{l=1}^{N} f_l e^{-M_l Q^2} e^{i\mathbf{Q}.\mathbf{r}_l} = |F|\, e^{i\varphi} \tag{2}$$

where $f_l(\mathbf{Q}, E) = f_l^0 + f_l' + if_l''$ and $e^{-M_l Q^2}$ is the x-ray diffraction Debye-Waller factor. For the sake of simplicity, we will assume that the complex atomic scattering factors $f(\mathbf{Q}, E)$ of all atoms *corresponding to the same element* are equal.

According to the schematic representation in Fig. 2, the scattered intensity from the crystal structure can then be written by separating the resonant scattering contribution of all anomalous atoms from the non resonant one:

$$I(\mathbf{Q}, E) \propto |F(\mathbf{Q}, E)|^2 = \left| F_T + F_A \frac{f_A' + if_A''}{f_A^0} \right|^2 \tag{3}$$

where F_T denotes the total structure factor excluding the terms coming from the resonant terms f_A' and f_A''. F_A corresponds to the Thomson scattering of anomalous atom A only.

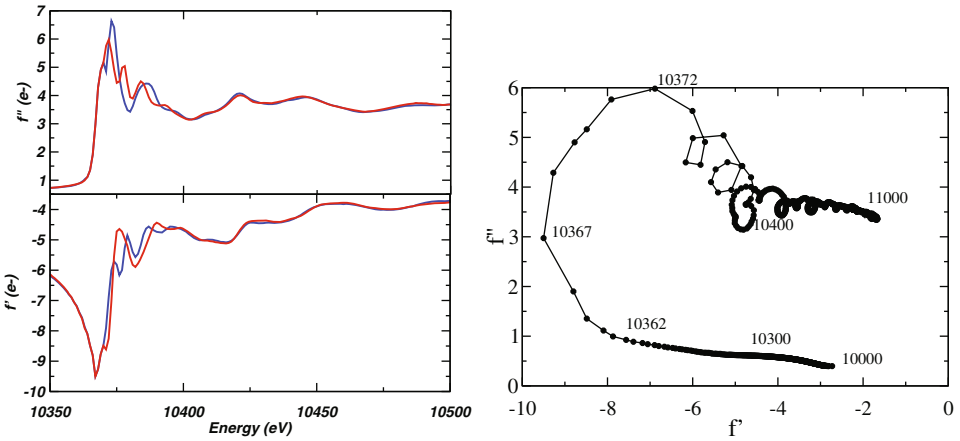

Fig. 1. Resonant scattering factors for gallium atoms in GaN: (top left) f''_{Ga} and (bottom left) f'_{Ga}, both given for an incident X-ray beam parallel (blue) and perpendicular (red) to the (0001) direction, with a strong anisotropy. (right) f''_{Ga} as a function of f'_{Ga}, represented in the complex plane. The energies used in a multiwavelength (GIMAD) resonant experiment should cover the largest area of the loop to yield the highest sensitivity. The small loops appearing in the energy range 10372–11000 eV, above the absorption edge (10367 eV), correspond to the Fine Structure, which is exploited in DAFS experiments (see Sect. 3).

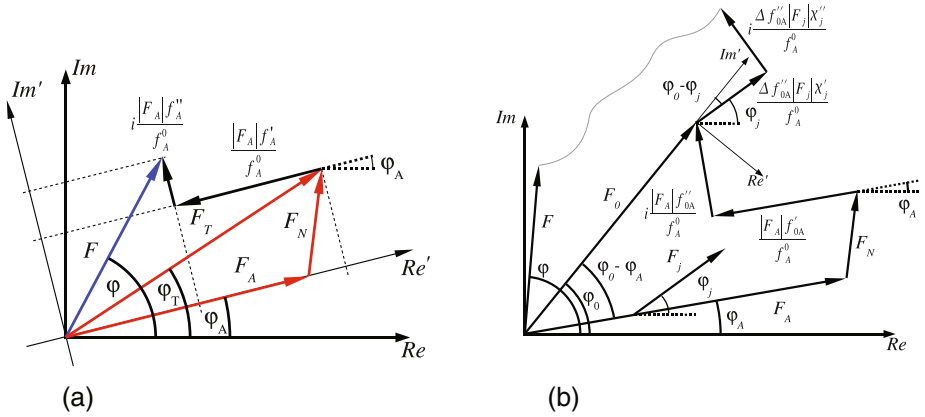

Fig. 2. (a) Principle of Multiwavelength Anomalous Diffraction: schematic representation in the complex plane of the structure factor F, and its relationship with the partial structure factors F_T, F_A and F_N. The scattered amplitude (F_T) is separated into the partial structure factors of the resonant atoms (F_A), and the non-resonant atoms (F_N). F_T represents the total scattered amplitude, excluding the resonant scattering of the resonant atoms (i.e. all terms which include f'_A and if''_A). (b) Schematic representation of first order contribution of χ'_j and χ''_j to structure factor F and to the Extended Diffraction Anomalous Fine Structure oscillations. The wavy curve stands for all other atomic oscillatory contributions. F_0 is the total structure factor excluding the fine structure oscillations.

The classical [2] MAD equation, giving the relationship between the intensity and the photon energy, can then be written as:

$$I(\mathbf{Q},E) \propto |F_T|^2 + (f'^2_A + f''^2_A)\left|\frac{F_A}{f^0_A}\right|^2 + \frac{2|F_T F_A|}{f^0_A}\left[f'_A\cos(\varphi_T-\varphi_A) + f''_A\sin(\varphi_T-\varphi_A)\right] \tag{4}$$

where φ_T (resp. φ_A) is the phase of the complex partial structure factor F_T (resp. F_A). An equivalent formula, detailing the fine structure factors in the resonant terms, will be presented in Sect. 3.

One can also write another useful expression for the scattered intensity by decomposing F_T in two contributions: $F_T = F_A + F_N$, where F_N is the partial structure factor corresponding to all *non* anomalous atoms:

From Fig. 2(a) one readily writes:

$$I(\mathbf{Q},E) \propto |F_N|^2 + \left[(f_A^0+f_A')^2 + f_A''^2\right]\left|\frac{F_A}{f_A^0}\right|^2 + \frac{2|F_N F_A|}{f_A^0}\left[(f_A^0+f_A')\cos(\varphi_N-\varphi_A) + f_A''\sin(\varphi_N-\varphi_A)\right] \quad (5)$$

where φ_N is the phase of the complex partial structure factor F_N.

In Eq. (4), f_A^0, f_A' and f_A'' are known, so that the three unknowns remain: F_T, F_A and $\Delta\varphi = \varphi_T - \varphi_A$. These can be determined if the scattered intensity is measured for at least three energies around the absorption edge. Different strategies then apply:

- in structural biology, a large number of reflections ($> 10^4$) is measured, and therefore the goal is to minimize the crystal exposure to X-rays, while determining a reasonably good starting value for F_A and most importantly $\Delta\varphi$.
- for semiconductor nano-structures, a scattering map is collected around one or a few reflections. Moreover, the unit cell structure is known, and therefore so is $\Delta\varphi$, so that a measurement at two energies can be enough to determine the composition, as was shown by the works of Magalhães-Paniago, Schülli, Malachias and co-workers [41–43]. However, this is only true as long as the nano-objects can be decomposed in *iso-strain* regions [33], i.e. in practice when the objects are large enough, and present large strain gradients. For smaller or buried objects, no *a priori* values can be assumed for $\Delta\varphi$ and at least 3 energies must be used.

In practice, data collection of GIMAD data is relatively fast (a few seconds per point of a *hkl*-scan combined to a 1D or 2D detector to produce a 2D or 3D map-, each *hkl*-scan taking a few minutes), so that it is advantageous to use a dozen of energies in order to improve the accuracy of the determination of F_T, F_A and $\Delta\varphi$. A program allowing the data extraction has been specifically developed for GIMAD data [44].

Two other points must be taken into account when considering *grazing incidence* diffraction:

- Distorted Wave Born Approximation effects [45]: the incident X-ray beam is reflected on the substrate surface, so that the scattering of objects above the surface can proceed either directly or through reflections above or below the surface. The reflection coefficients must then be taken into account, although it does not affect the validity of Eq. (4).
- If the substrate contains anomalous atoms [46] or if the objects above the surface are thick enough, the absorption correction and/or the dependence of the reflection coefficients on the photon energy must be taken into account. Calculating this correction can be difficult if the substrate includes a high percentage of resonant atoms; however it was shown that it is also possible to use an internal standard to achieve this [46].

3 Diffraction anomalous fine structure

3.1 EDAFS to first order

In the extended region above the edge, the anomalous atomic scattering factor can be split into *smooth* and *oscillatory* parts: $f'_j = f'_{0A} + \Delta f''_{0A}\chi'_j$ and $f''_j = f''_{0A} + \Delta f''_{0A}\chi''_j$, where $f'_{0A} + if''_{0A}$ is the anomalous scattering of bare neutral atoms and $\Delta f''_{0A}$ is the contribution of the resonant scattering to f''_{0A}. The smooth atomic scattering factor is: $f_{0A}(\mathbf{Q}, E) = f^0_A + f'_{0A} + if''_{0A}$.

The real and imaginary components of the complex extended diffraction anomalous fine structure $\tilde{\chi} = \chi'_j + i\chi''_j$, are related by the Kramers-Kronig transforms and the imaginary component χ''_j is related to EXAFS χ_j by the following equation: $\chi_j(E) = Im\tilde{\chi}(\mathbf{Q} = 0, E)$.

One can write the structure factor as follows:

$$F(\mathbf{Q}, E) = F_0(\mathbf{Q}, E) + \frac{\Delta f''_{0A}(E)}{f^0_A(Q)} \sum_j F_j(\mathbf{Q})[\chi'_j(E) + i\chi''_j(E)] \tag{6}$$

to first order, the intensity can be written:

$$I(\mathbf{Q}, E) = FF^* \approx I_0 + 2\frac{\Delta f''_{0A}\,|F_A|\,|F_0|}{f^0_A}\chi_{\mathbf{Q}} \tag{7}$$

where $F_0 = |F_0|\, e^{i\varphi_0}$, $I_0 = |F_0|^2$, $\chi_{\mathbf{Q}}$ is first order Extended DAFS:

$$\chi_{\mathbf{Q}} = S_D\left[\frac{I - I_0}{I_0}\right] = \cos(\varphi_0 - \varphi_A)\sum_{j=1}^{N_A} w'_j\chi'_j + \sin(\varphi_0 - \varphi_A)\sum_{j=1}^{N_A} w''_j\chi''_j \tag{8}$$

$S_D = \frac{f^0_A|F_0|}{2\triangle f''_{0A}|F_A|}$ is a normalization factor. By inspection of Eq. (4) and Fig. 2, one readily sees that the knowledge of $\beta_{TA} = \frac{|F_A|}{f^0_A|F_T|}$ and $\varphi_T - \varphi_A$ is sufficient to determine S_D and the phase difference $\varphi_0 - \varphi_A$, i.e. there is no need for a crystallographic model.

$$S_D = \frac{|F_0|}{|F_T|}\left[\frac{1}{2\beta_{TA}\Delta f''_{0A}}\right] \tag{9}$$

$$\tan(\varphi_0 - \varphi_A) = \frac{\sin(\varphi_T - \varphi_A) + \beta_{TA}f''_{0A}}{\cos(\varphi_T - \varphi_A) + \beta_{TA}f'_{0A}} \tag{10}$$

where

$$\frac{|F_0|}{|F_T|} = \left[\cos(\varphi_T - \varphi_A) + \beta_{TA}f'_{0A}\right]^2 + \left[\sin(\varphi_T - \varphi_A) + \beta_{TA}f''_{0A}\right]^2. \tag{11}$$

Equation (10) shows that phase φ_0 depends on the energy. The crystallographic weights

$$w'_j = \frac{|F_j|\cos(\varphi_0 - \varphi_j)}{|F_A|\cos(\varphi_0 - \varphi_A)} \tag{12}$$

and

$$w''_j = \frac{|F_j|\sin(\varphi_0 - \varphi_j)}{|F_A|\sin(\varphi_0 - \varphi_A)} \tag{13}$$

represent the orthogonal projections of χ'_j and χ''_j on the vector F_0 in the complex plane (see Fig. 2), $\sum_{j=1}^{N_A} w'_j = \sum_{j=1}^{N_A} w''_j = 1$. One can calculate them provided that the

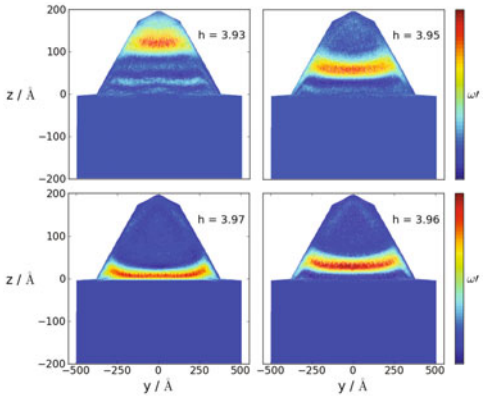

Fig. 3. Spatial selectivity of a diffraction experiment, shown for a simulated *GeSi* uncapped dome grown on *Si(001)* (see Sect. 5.1). The two-dimensional maps represent the diffraction weights $w'_{j=Ge}$ for different $\boldsymbol{Q}(h,0,0)$ vectors with $h = 3.97$, 3.96, 3.95 and 3.93. Decreasing h corresponds to increasing the height z of the scattered region in Bragg condition. The weights are summed along the [100] direction and plotted in the yz plane.

crystallographic structure is known, or determine them if the individual $\chi'_j(\chi''_j)$ are known by fitting Eq. (8) to the experimental $\chi_{\mathbf{Q}}$. Note that $\sum_{j=1}^{N_A} w''_j \chi''_j$ is to be compared to the Extended XAFS oscillations which can be written $\chi_{EXAFS} = \sum_{j=1}^{N_A} \chi''_j$. The fundamental difference are the weights w''_j that give DAFS site/spatial selectivity.

As an example we have calculated the EDAFS weights for a GeSi uncapped dome grown on Si(001) (see Sect. 5.1). The {dome + substrate} structural model was obtained by atomistic simulations that are shown in the following Sect. [47]. As expected, the uncapped dome relaxes in the growth direction (z axis), i.e. the in-plane lattice parameter increases with z. Therefore decreasing the in-plane reciprocal unit $h = 4(1-\varepsilon)$ in reciprocal space close to the Si 400 reflection, where ϵ is the island in-plane strain ($\varepsilon > 0$), means selecting a region of the island at a higher z value above the Si surface.

Figure 3 shows the relative contribution (w'_j) of the real part χ'_j of an individual Ge atom j to the total χ' oscillations, for different h values, calculated for the structural model. The iso-strain regions along the z direction are clearly put in evidence as a function of h. Also, one can observe a broadening going from the interface to the top of the dome. The maps give a direct and quantitative estimation of the spatial resolution in the z direction showing that a high resolution is achieved at the interface.

3.2 EDAFS path formalism

Using the paths formalism [48], the *complex extended fine structure* that depends on the local atomic environment of a resonant atom j is [4, 49]:

$$\chi'_j + i\chi''_j = -\sum_{\gamma=1}^{\Gamma_j} A_{\gamma j}(k) e^{-i(2kR_{\gamma j} + \varphi_{\gamma j}(k))}. \tag{14}$$

The sum runs over all scattering paths γ of the virtual photoelectron, $k = \frac{1}{\hbar}\sqrt{2m_e(E-E_0)}$ is the photoelectron wavenumber, E_0 the edge energy, $R_{\gamma j}$

the effective length of path γj and $\varphi_{\gamma j}(k)$ the net scattering photoelectron phase shift.

Equations (8) and (14) lead to the following $\chi_{\mathbf{Q}}(k)$ expression:

$$\chi_{\mathbf{Q}}(k) = \sum_{j=1}^{N_A} \frac{|F_j|}{|F_A|} \sum_{\gamma=1}^{\Gamma_j} A_{\gamma j}(k) \sin\left(2kR_{\gamma j} + \varphi_{\gamma j}(k) + \varphi_0(k) - \varphi_j - \frac{\pi}{2}\right). \tag{15}$$

When the virtual photoelectron probes similar local atomic environments for all resonant atoms j (as for instance Ge atoms in GeSi/Si(001) islands), one can set $A_{\gamma j} = A_\gamma$, $\varphi_{\gamma j} = \varphi_\gamma$ and average on photoelectron scattering paths γj over all j sites. So, in Eq. (8) one can write:

$$\sum_{j=1}^{N_A} w'_j \cos\left(2kR_{\gamma j} + \varphi_{\gamma j}\right) = e^{-2k^2\sigma_\gamma^2} \cos\left(2k\left\langle R\right\rangle_\gamma + \varphi_\gamma\right) \tag{16}$$

where $\langle R\rangle_\gamma$ is the average effective length of path γ and σ_γ the bond-length disorder (static and dynamic Debye-Waller factors). A similar expression is obtained with the sine terms. Note that the same kind of averaging is performed in the case of EXAFS but here a weighting of the γj paths is performed by w_j factors which express the diffraction condition, and allow one to select an isostrain region of the sample as shown in Fig. 3.

Then, Eq. (8) can be written in a simple form:

$$\chi_{\mathbf{Q}}(k) = \sum_{\gamma} A_\gamma(k) e^{-2k^2\sigma_\gamma^2} \sin\left(2k\langle R\rangle_\gamma + \varphi_\gamma(k) + \varphi_0(k) - \varphi_A - \frac{\pi}{2}\right). \tag{17}$$

In Eq. (17), the $\chi_{\mathbf{Q}}$ expression is very similar to the EXAFS one, the only difference being the crystallographic phase $\Delta\psi = \varphi_0(k) - \varphi_A - \frac{\pi}{2}$ in the sine argument.

3.3 DAFS and EDAFS data reduction and analysis

In this section we address DAFS data reduction and show how to recover precise information on the composition by analysing the cusp (or line-shape) of a DAFS spectrum. As shown in Sect. 2, the MAD method allows to extract the partial structure factors F_A, F_N and phase difference $\varphi_N - \varphi_A$ by measuring diffraction curves (or maps in reciprocal space) at several energies in the vicinity of an absorption edge of one element (the resonant atom) that belongs to the nanostructures. This method provides a powerful way to discriminate, in reciprocal space, the resonant atoms scattering (its modulus). Then one can recover *model-free parameters* as the actual strain and size of the nanostructures [28,29,50,51] as well as the composition in the case of a binary alloy.

Fitting Eq. (5) to a DAFS spectrum cusp is equivalent to performing a MAD fit (see Sect. 2) with a very detailed data as a function of energy and on a wider energy range as shown in Fig. 4. It gives very precise values of $\frac{|F_A|}{|F_N|}$ and $\varphi_N - \varphi_A$. In the case of a *homogeneous binary alloy*, $\varphi_N - \varphi_A = 0$ and the ratio $\frac{|F_A|}{|F_N|}$ readily gives the amount of intermixing. So, it is convenient to combine MAD and "iso-strain scattering" methods (see Sect. 5) to recover the composition in the iso-strain regions picked up by the diffraction condition. The method still applies when $\varphi_N - \varphi_A \neq 0$ provided that one can assume that $|F_A|$ (resp. $|F_N|$) is proportional to the number of A (resp. N) atoms. In the most general case, the crystallographic structure must be used to fit DAFS spectrum and refine the occupation factor of the resonant atoms [5,16,24,25].

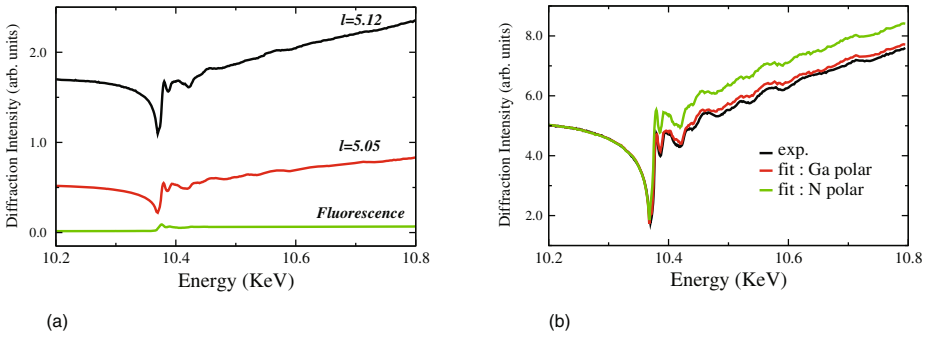

Fig. 4. (a) *AlGaN* nanowires grown on *Si(111)* (see Sect. 5.2). Raw DAFS spectra measured at $h = 1.03$, $l = 5.12$ and $h = 1.03$, $l = 5.05$ ($k = 0$) and fluorescence yield (all data are normalized to the incoming beam intensity $I_{mon.}$). (b) Experimental DAFS spectrum measured at $h = 1.03$, $l = 5.05$ ($k = 0$), corrected for fluorescence. The fit curves were obtained with the experimental f'_{Ga} and f''_{Ga} and the $Al_{1-x}Ga_xN$ wurtzite structure for the *N*- and *Ga*- polarities. Only the *Al* content $1 - x$ was refined. No absorption correction was applied.

3.3.1 Data measurement and reduction

For the sake of simplicity and pedagogy, we show hereafter the data reduction and analysis of DAFS spectra obtained for AlGaN/Si(111) nanowires (NWs, see Sect. 5.2). The experiment was performed at the French Collaborative Research Group (CRG) beamline BM2 at the European Synchrotron Radiation Facility (ESRF). Intensities of symmetric Bragg reflections, i.e. with equal incident and exit angles, were measured with an 8-circle diffractometer (Euler geometry). The diffraction vector was in the *vertical* plane, i.e. the incoming and diffracted beam polarization vectors were (stayed) perpendicular to the diffraction vector. Beam size at the focal point was about $0.3 \times 0.15\,\text{mm}^2$, thus illuminating a large assembly of NWs. Scattered intensity was recorded by a linear gas-detector (Vantec^{TM}) spanning over an exit angle range of about [0–2°] and the incident X-ray beam was monitored by a dedicated photodiode ($I_{mon.}$) [19].

DAFS spectra were measured at the Ga K-edge (10367 eV), intensities were recorded over an energy range of 1000 eV and with an energy step size of 2 eV before the edge and $0.06\,\text{Å}^{-1}$ in k-space after the edge. The background intensity (mainly fluorescence) was additionally monitored in order to correct the data for the fluorescence and diffuse scattering signals. Also, *very important*, the fluorescence data was used to obtain experimental f'_{Ga} and f''_{Ga} curves to be used for fitting DAFS data. So, the optical transfer function, including the monochromator resolution, and the finite lifetime of the virtual excited state is correctly taken into account. Finally, the crystallographic structure of nitride compounds being hexagonal (wurtzite structure), f'_{Ga} and f''_{Ga} strongly depend on the orientation of the incoming and scattered beam polarisation vectors with respect to the hexagonal crystallographic axes [37,52,53]. It is *mandatory* to use experimental f'_{Ga} and f''_{Ga} to obtain reliable results.

Figure 4(a) shows raw DAFS spectra measured at $h = 1.03$, $l = 5.12$ and $h = 1.03$, $l = 5.05$ ($k = 0$) (see Sect. 5.2) together with the background intensity variations (mainly fluorescence yield) measured at $h = 1.07$, $l = 5.25$, close to the points in reciprocal space where DAFS spectra were measured. All data shown in Fig. 4 are the intensity integrated over the linear detector, $I_{diff.}$, and normalised to the incoming beam intensity $I_{mon.}$: $I_{diff.}/I_{mon.}$. Given the amount of Ga atoms in the sample, the fluorescence yield is weak and, most importantly, the jump at the Ga K-edge is small in comparison with the anomalous diffraction intensity variation. Resonant

scattering factors f' and f'' were obtained in two different ways. For Al and N atoms we used the theoretical values obtained with the *Cromer* and *Liberman* program [54]. For Gallium atoms, the experimental f''_{Ga} was obtained by scaling the fluorescence intensity (normalized to the incoming beam intensity and multiplied by the incoming beam energy, see for instance [55]) to the theoretical f''_{Ga}. Then, we used the Kramers-Kronig transforms to calculate f'_{Ga} [55,56]. All calculations were performed with the *DIFFKK* software [48].

DAFS intensity is related to the square modulus of the structure factor according to the following formula:

$$I(\mathbf{Q},E) = KD(E)L(\mathbf{Q},E)PA(\mathbf{Q},E)\left|F(\mathbf{Q},E)\right|^2 \tag{18}$$

where I is corrected for the background intensity (mainly fluorescence), K is a scale factor, D the detector efficiency, L and P the Lorentz and polarization factors for Thomson scattering, A the absorption correction. $F(\mathbf{Q},E)$ is the structure factor calculated in the Born Approximation (incident/outgoing wide angles). The D factor takes into account the whole detection set-up, comprising the detector efficiency and absorption all the way from the monitor to the diffraction detector. It is not always possible to perform a direct measurement of the base-line, without inserting attenuators in the direct beam. However, the energy dependence of D is often linear inside the energy range of interest, so that D may be fitted to DAFS spectrum with a straight line ($D = m(\Delta E + 1)$), where m is the only adjustable parameter, $\Delta E = E - E_0$, and E_0 is the edge energy. In some cases, a parabolic dependency, correlated to the beam defocusing as a function of the energy, is necessary.

Care must be taken to measure DAFS spectrum far enough from the absorption edge up to the point where anomalous scattering is negligible, otherwise the m parameter is correlated to crystallographic phase $\varphi_T - \varphi_A$. For a rotation scan, i.e. with the rotation axis perpendicular to the plane of incidence (containing the incident (resp. outgoing) $\mathbf{k}$ (resp. $\mathbf{k}'$) vector, $\mathbf{Q} = \mathbf{k}' - \mathbf{k}$), $L = \frac{\lambda^3}{\sin 2\theta}$ (for the calculations of Lorentz factor see for instance [55]). The polarisation correction for the Thomson scattering is given by the dot product $\boldsymbol{\varepsilon}_\mu.\boldsymbol{\varepsilon}^*_{\mu'}$ where $\boldsymbol{\varepsilon}_\mu(\boldsymbol{\varepsilon}^*_{\mu'})$ is the polarisation vector of the incoming (outgoing) beam. At a bending magnet, the polarization of the beam that propagates in the electron orbit plane, is linear and perpendicular to the vertical plane of incidence (containing $\mathbf{k}$ and $\mathbf{Q}$) that was used for all experiments reported hereafter, then $\boldsymbol{\varepsilon}_\mu.\boldsymbol{\varepsilon}^*_{\mu'} = 1$. Also, with this scattering geometry the polarisation dependence of f'_{Ga} and f''_{Ga} are the same for the incoming and scattered beams and do not change as function of $\mathbf{Q}$ and the energy. It is worth noting that in principle L and D do depend on the X-ray beam energy, however these functions vary smoothly at the scale of DAFS energy range.

3.3.2 Absorption correction

The absorption correction A depends on the energy, it lowers the intensity level after the edge. For bulk samples the effect is very strong and "kills" DAFS signal. The great advantage of nanostructured samples is that the absorption correction is weak if not negligible. In symmetric Bragg geometry and for an incident beam projection area not greater than the sample surface area, the absorption of a thin film of thickness t is:

$$A(\mathbf{Q},E) = \frac{1}{\sin\alpha}\int_0^t e^{-2\mu t/\sin\alpha}dz = \frac{1-\exp(-2\mu t/\sin\alpha)}{2\mu} \tag{19}$$

where α is the incidence angle and μ is the linear absorption coefficient. The absorption correction takes into account the change of the X-ray beam footprint area as a function of α.

3.3.3 Non centrosymmetric structure. Polarity

In the case of a *non centrosymmetric* structure one must remember that Friedel's law is no longer valid: $(I(hkl) \neq I(\bar{h}\bar{k}\bar{l}))$ and that the difference in the diffracted intensity of Bijvoet pairs[1] of reflections can be significant and measurable when resonant effects (f'') are not negligible. This effect is very strong in the case of nitride compounds which grow with the wurtzite structure (space group $P6_3mc$, polar structure), and has been recently used to determine the polarity of GaN/Si(111) NWs [58]. Polarity is defined by considering the orientation of Ga-N bonds that are collinear with the c-axis of the wurtzite cell. The vector going from Ga and pointing towards N conventionally defines the [0001] direction. A structure is said to be Ga-polar or Ga-terminated when its growth direction is [0001]. Reciprocally, a crystallographic structure is said N-polar when its growth direction is $[000\bar{1}]$. The main effect on DAFS spectra measured with Bijvoet reflections is the relative change in intensity after the edge. This is simply because $\phi_T - \phi_A$ is changed into its opposite $\varphi_A - \varphi_T$ (note that it is not exactly true when taking into account the weak anomalous scattering of the non resonant atoms). Therefore, in a first approximation Bijvoet reflections will give about the same composition, but to obtain an unbiased value, polarity must be taken into account.

At this point it is worth noting that we have mentioned above three effects that modify the intensity level at and above the edge: *fluorescence* (increase), *absorption* (decrease) and *non centrosymmetry* as in the case of *polar wurtzite structure* (decrease or increase).

3.3.4 Data refinement

The cusp of DAFS spectra, corrected for background intensity and absorption, is given by the energy dependence of $|F(\mathbf{Q}, E)|^2$. Knowing the crystallographic structure as well as f' and f'', the fit of Eq. (18) to DAFS spectrum allows one to refine the occupation factor of the resonant atoms. See Sect. 5.1 which reports the study of GeSi binary alloy for which the knowledge of the crystallographic structure is not necessary *a priori* for determining the composition.

To obtain the correct Al content in AlGaN NWs (wurtzite structure), the strategy is as follows: Equations (18) and (4) are fitted to DAFS spectra corrected for fluorescence, in the whole energy range, ignoring absorption and polarity at first. This gives the geometrical parameters K and $D(E)$ as well as values of $\frac{|F_A|}{f_A^0|F_T|}$ and $(\varphi_T - \varphi_A)$, the latter being affected by absorption and polarity. Then, the Al occupation factor is refined with the structure factor calculated with the wurtzite structure by fitting Eq. (18) to DAFS spectra in the energy range only *below the edge*.

Figure 4(b) shows the experimental DAFS spectrum measured at $h = 1.03$ and $l = 5.05$ $(k = 0)$, corresponding to the Ga-rich AlGaN NWs, together with the fit curves for the N-polar and Ga-polar orientations. To determine the polarity we must take into account self absorption, which is small but not negligible because the NWs are Ga rich, $0.7\mu m$ long and dense. According to expression 19 for $A(E)$, the fit of Eq. (18) to the DAFS spectrum (in the whole energy range), with Ga-polar orientation, gives an effective absorption length $t/\sin\alpha$ $(\alpha = 34°)$ equal to $470nm$. This value is correct whereas in the case of a fit with N-polar orientation the effective absorption

[1] Friedel pairs refer to reflections with Miller indices hkl and $\bar{h}\bar{k}\bar{l}$ while Bijvoet pairs [57] more generally refer to pairs of reflections which are symmetry-related (including the additional inversion center), but have different intensities (i.e. Friedel's law does not hold).

length $t/\sin\alpha$ is much too large. Therefore AlGaN NWs are Ga-polar and the Al content is equal to 0.11. In contrast with GaN NWs grown on Si(111) [58], the polarity of AlGaN NWs is tentatively assigned to the simultaneous exposure of Si(111) surface to both Ga and Al.

Last but not least, the fitting of DAFS spectrum cusp (corrected for fluorescence and absorption) gives the scale factor S_D (Eq. (9)) and the crystallographic phase $\varphi_0 - \varphi_A$ (Eq. (10)) which are used to analyse first order EDAFS oscillations (see Sect. 3.1). Normalisation of the experimental EDAFS oscillations can readily be obtained by mutiplying S_D to the EDAFS extracted signal $\frac{I-I_0}{I_0}$ (where I_0 is the diffracted intensity without oscillations).

4 Applications of MAD to study semiconductor nanostructures

4.1 Composition of Ge quantum dots (QDs) deposited on silicon

The GIMAD technique has been used for the study of a large number of nanostructures: it is particularly interesting in the case of *epitaxial nano-structures*, as there is a wide range of synthesis parameters: growth mode (Stranski-Krastanow, Volmer-Weber for quantum dots, Vapor-Liquid-Solid for nanowires, etc...), temperature, flux of the components, type of deposition (Molecular Beam Epitaxy, Molecular-Organic Chemical Vapor Deposition), etc...

All these parameters can alter the result of the synthesis, particularly regarding the shape of the grown objects, their strain field (relaxation with or without plastic defects), and interdiffusion between the grown nano-structures, the substrate and/or the capping material.

Among semiconductor nano-structures, Germanium deposited on Silicon is one of the most studied systems. In this example [59], ≈ 6 monolayers of Germanium where deposited on a Si (001) substrate at $T = 650°$C, yielding fairly monodisperse Germanium domes [60], with a height of ≈ 20 nm and a diameter around 120 nm.

In order to determine the degree of the interdiffusion between Ge and Si, GIMAD was performed at the CRG BM02 beamline of the European Synchrotron Research Facility [19]. Radial scans (along the [100] direction) were measured around the 400 in-plane reflection of the silicon substrate using 12 different photon energies around the Germanium K-edge at $E = 11.103$ keV. The incident angle was $\alpha_i = 0.12°$, below the silicon critical angle at $\alpha_c = 0.16°$, in order to enhance the scattering signal from the islands rather than that of the silicon substrate.

The 12 radial scans were processed using the NanoMAD program [44], and the results are shown in Fig. 5: it is possible to extract the partial structure factors from Si and Ge as a function of the h coordinate in reciprocal space, and henceforward the relative composition of Germanium can be extracted (Fig. 5(b)).

As the Ge islands are relatively large, it can be decomposed in so-called iso-strain layers [33], each diffracting at a diffrent h value. Effectively, this means that the composition vs. h corresponds to the variation of the composition with the height in the island. Although it is beyond the scope of this article, it should be noted that it is also possible to determine the lateral size of each iso-strain layer, by performing an angular scan for each considered h value (see [43] for more details), and henceforward obtain a more complete 3D view of the shape, composition and strain in the dots.

Finally, we measured 2D scattering maps by GIMAD and performed the same MAD data analysis, as reported for the in-plane 400 reflection, on the same type of sample, at ID01 beamline of ESRF. The 602 reflection was measured in grazing incidence at 12 energies close to the Ge K-edge using a 1D Vantec^{TM} detector. The corresponding 2D map with the Ge partial structure factor is shown in Fig. 6. It was

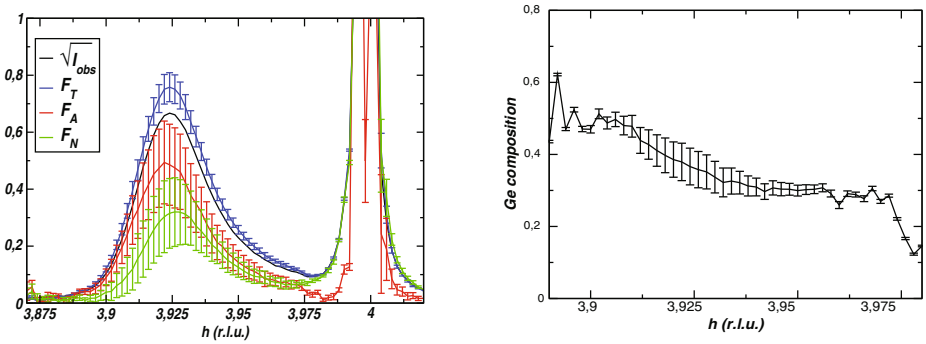

Fig. 5. (a) Scattered amplitude along the radial direction ([100] direction), around the 400 reflection, at $\alpha_i = 0.12°$, with the data extracted from GIMAD data: raw amplitude at $E = 11$ keV (black), total (blue) and partial structure factors for Ge (red) and Si (green). (b) Ge composition (in percent), as extracted from GIMAD data, as a function of h (r.l.u.). The sharp peak at $h = 4$ corresponds to the Si substrate. The broad peak at lower h values corresponds to the Ge QDs, the peak profile is related to the strain gradient inside the dots and must be evaluated by taking into account multiple reflections at the substrate surface, using the Distorted Wave Born Approximation (DWBA) [33,45,59].

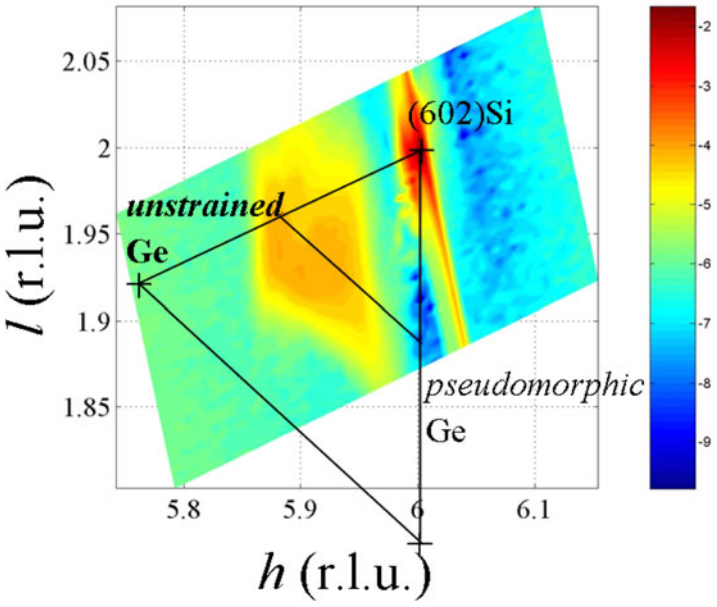

Fig. 6. Diffraction map recorded around the 602 reflection, using a grazing incident angle. The 2D map was recorded using a 1D Vantec^{TM} detector, at 12 energies around the Ge K-edge – in this image is shown only the partial structure factor F_{Ge} [61].

interpreted by comparison with calculated maps obtained by using an elastic model. The results are given in reference [61].

4.2 Example 2: Strain relaxation in GaN quantum dots capped with AlN

GaN nano-structures have recently attracted considerable interest, in view of a wide range of applications due to their photo-luminescence properties (with or without doping) around the visible range.

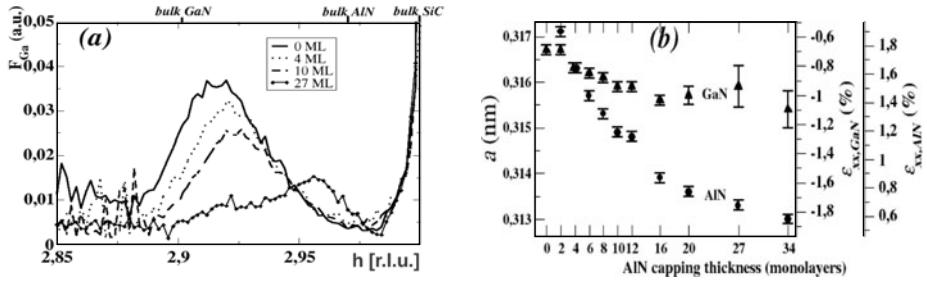

Fig. 7. GIMAD on GaN quantum dots: (a) data for one layer of GaN quantum dots capped with AlN layers of various thicknesses. The extracted F_{Ga} allows to determine the average in-plane strain in the GaN QD. (b) Evolution of the in-plane strain (ε_{xx}) for GaN and AlN as a function of the number of AlN capping layers deposited.

In this example [50], ≈ 6 monolayers of GaN were deposited on a buffer layer of AlN, grown on a SiC substrate, using a modified Stranski-Krastanov growth mode [62], yielding GaN quantum dots with an average height of ≈ 3 nm and a diameter of ≈ 15–20 nm. Then, several samples were grown with different thicknesses of AlN as capping layer above the GaN quantum dots, in order to study the relaxation process as a function of the capping thickness.

In order to separate the scattering from GaN and AlN, GIMAD was performed at 12 energies around the Ga K-edge at $E = 10.367$ keV. The extracted partial structure factor from Ga is shown in Fig. 7(a), clearly exhibiting the shift of the average strain in the GaN islands as more layers of AlN are added. Compared to the Ge/Si system, it is not possible to decompose the signal in iso-strain regions, due to the much smaller size of the islands.

In Fig. 7(b) the average in-plane strain is plotted as a function of the thickness of the capping AlN layer – the average strain state of the AlN layer was also extracted. It shows that the strain state of the AlN capping layers is influenced by the underlying GaN QDs up to a thickness of 30 ML. This leads to a strained crystalline surface up to 30 ML of capping material, which explains the vertical correlation observed when stacking several layers of GaN QDs [50,63].

5 Combining MAD and DAFS to study semiconductor nanostructures

In this section we report on a few examples of the application of MAD and DAFS to the structural study of semiconductor nanostructures. We chose the case of free standing Ge/Si nanoislands and AlGaN nanowires (NWs). These two systems are quite different from each other both morphologically and concerning their physical properties. Also, in the first example, Grazing Incidence geometry was necessary whereas for the NWs we used a large incidence.

In the case of Ge/Si the main issue is to determine the actual composition of the islands, due to the very strong intermixing effect with the Si atoms of the substrate during growth. This unique combination of GIMAD, GIDAFS and theoretical simulations, is shown to disentangle strain and composition, to probe the average Ge composition especially in the region of the substrate/island interface and thus to elucidate the vertical compositional profile inside dome-shaped islands.

III-Nitrides instead, are scarcely affected by unwanted intermixing of the III group elements. Nevertheless the growth of ternary Nitrides (such as AlGaN) is complicated

due to the great difference between Al and Ga diffusion coefficients, and the composition can be quite inhomogeneous. Composition gradients can appear, modifying the optical properties of the material. Moreover this example is quite didactic since it shows a very direct application of the simultaneous chemical/site selectivity of the technique and its immediate sensitivity to the presence of composition gradients. These examples also serve to illustrate DAFS spectra reduction and analysis (see Sect. 3.3).

5.1 Ge/Si nanoislands

GeSi nanostructures have been widely studied, from the beginning of semiconductor research, on one hand for device applications and integration on Si-based technology [64,65], and on the other hand, as a model system for semiconductor alloys. Their composition has been experimentally studied by various techniques such as quantitative high-resolution Transmission Electron Microscopy (TEM) [66], X-ray Energy Dispersive Spectrometry (XEDS) [67], X-ray Absorption Fine Structure spectroscopy [68], Anomalous X-Ray Diffraction (AXRD) [41–43,69,70] and by combining selective wet chemical etching with Atomic Force Microscopy (AFM) [71].

Using these techniques, a strong effect of Ge-Si intermixing giving different composition profiles [71–73] has been reported. The general view emerging from these studies is that surface diffusion (*i.e.* migration of Si and Ge adatoms at the surface) must be regarded as the most active process to explain intermixing. Reference [74] gives an exhaustive review of previous investigations on compositional mapping in SiGe islands.

5.1.1 Experimental

The sample studied here was grown by Molecular Beam Epitaxy (MBE). Dome-shaped islands were obtained by depositing 5.5 monolayers (ML) of Ge at 650 °C on a flat Si(001) substrate with a Ge growth rate of 0.03 Å/s. AFM analysis shows that the domes are rather homogeneous in size with an average height of 19 nm and a diameter of about 80 nm, respectively.

Grazing incidence MAD and DAFS measurements were performed at beamline BM02 and ID03 at the ESRF, Grenoble, and analysed as described in previous papers [19,30,75]. The measurements were performed *ex situ* in vacuum environment after growth. An amorphous oxide layer is possibly present but it would not extend by more than $2nm$ from the top surface, thus having no influence on the reported results. All direct or reciprocal space notations below refer to the bulk Si unit cell ($a = b = c$ =5.431 Å, $\alpha = \beta = \gamma = 90°$). The Miller indexes h, k and l are expressed in reciprocal lattice units (r.l.u.) of bulk Si.

The GIMAD (resp. GIDAFS) experiments were performed at the Ge K-edge (11.103 keV) at an incident angle $\alpha_i = 0.1°$ (resp. $\alpha_i = [0.2 - 0.25°]$). The Si critical angle α_c is 0.163° at 11 keV. Grazing incidence geometry was used to enhance the weak contribution of the islands with respect to that of the substrate. Scattered intensity was recorded by a linear gas-detector (Vantec^{TM}) and integrated over the exit angle α_f in the range of 0 to about 1.5°.

5.1.2 Atomistic simulations

We carried out an atomistic structural modelling of the {dome + substrate} system with the aim of improving the interpretation of the experimental data by simulating X-ray diffraction (see Fig. 8).

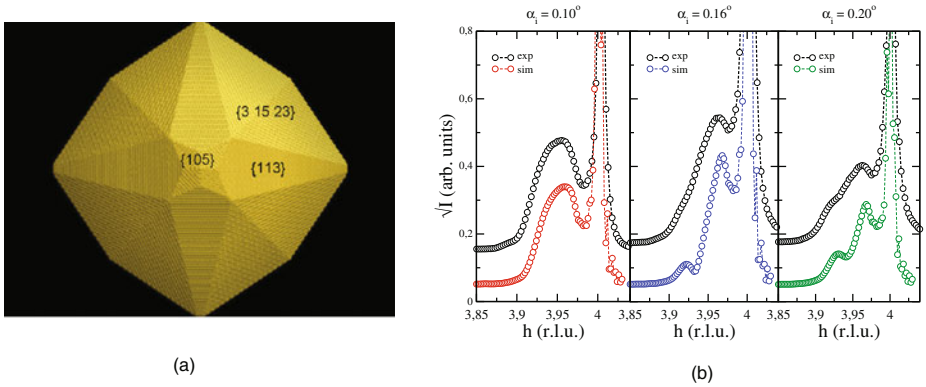

Fig. 8. (a) Perspective top view of the GeSi/Si(001) faceted dome-shaped structural model. The model has a diameter and height of 76 and 19 nm respectively, with a homogeneous chemical composition of 60% Ge, it is made of about 2 million of atoms. (b) Experimental (exp) and simulated (sim) square-root of the scattered intensity near the Si 440 reflection for incident angles near the critical angle.

The chemical composition profile was modelled as a step function, i.e. an abrupt Si substrate/dome interface and a homogeneous distribution in the Ge_xSi_{1-x} dome with $x = 0.6$ (see next section). The size of the island was set at the real dome size. Its morphology reproduces the dome shape, including faceting ({105}, {113}, {15 3 23}). The diameter and depth of the Si substrate volume included in the calculation were set to 1.3 (resp. 2.0) times the diameter (resp. height) of the dome. These optimized values were fixed after running several energy minimizations for different substrate sizes and a dome of smaller size than the experimental one but with the same aspect ratio (the relaxation state of the island depends essentially on this parameter [76]). The total number of atoms of the model was about 21 million, 2 million of which correspond to the dome. The system energy was described by the Tersoff potential [77]. At first, the atoms of both the dome and substrate were located at the bulk Si crystallographic sites. The energy minimization was carried out by means of parallel classical Molecular Dynamics, cooling down the system to nearly 0 K using *LAMMPS* code [78,79]. Periodic and fixed boundary conditions were applied to the lateral dimensions (x,y) of the substrate and to the deeper atomic plane of the Si substrate, respectively.

Once the relaxed cluster has been obtained all the individual atoms positions are defined, then one can calculate GIMAD, EDAFS oscillations and EDAFS weights, and compare them with experimental data. For instance, Fig. 8 shows that, in the present case, the agreement between experimental data and calculations is very good as far as GI X-Ray Diffraction is concerned. We have also shown in Sect. 3.1, as a matter of basic principles illustration, the simulated EDAFS weights ($w'_{j=Ge}$).

The composition profile has been also simulated by MAD formalism applied to the {dome+substrate} diffraction and compared to the experimental one obtained, as previously explained in Sect. 2, out of GIMAD h- (or h=k-) scans with the *NanoMAD* program [44,47]. The comparison is shown in Fig. 9.

One can see that the simulated GIMAD profile is not as sharp as the step function composition used for the model cluster, this means that the strained substrate underneath the domes smears out the composition profile extracted by MAD (in-plane diffraction probes the in-plane lattice parameter that is continuous at the interface). This is not only a straightforward result [27] but also a very important one: at the dome/substrate interface region, composition and strain can not be properly disentangled by in-plane MAD in the case of a sharp interface region. The simulated EDAFS

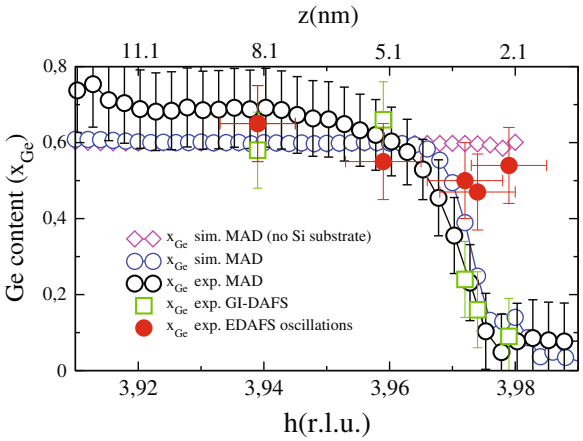

Fig. 9. Experimental Ge composition x_{Ge} determined by GIMAD (black open circles), by fitting GIDAFS cusp (green open squares) and EDAFS analysis (red filled circles). The experimental curves are compared with simulated MAD data (pink diamonds and blue circles) obtained taking into account the scattering of the dome, and the {dome + substrate}. The curves are plotted as a function of reciprocal unit h around Si 400 and height z above the sample surface.

weigths $w'_{j=Ge}$ shown in Sect. 3.1 to quantify the EDAFS spatial resolution in the real space, clearly put in evidence that the best resolution is obtained close to the interface, *i.e.* where MAD fails due to the scattering contribution of the strained Si substrate underneath the domes.

5.1.3 EDAFS results

We measured GIDAFS spectra at the Ge K-edge and analyzed the GI-Extended-DAFS oscillations that show up above the edge. The analysis of the EDAFS oscillations gives the short range order structural environment of Ge atoms inside the domes and allows one to determine, independently of MAD, the Ge content of the islands as a function of z above the sample surface. In particular we want to obtain composition in the region of the dome close to the dome/substrate interface. Figure 10 shows three DAFS spectra measured at different in-plane $\boldsymbol{Q}$ $(h,k,0)$ vectors which correspond to three iso-strain regions in the dome located at different heights z (Table 1) [47].

As stated in Sect. 3.3, in the case of a binary alloy one can use MAD formalism to obtain a *model free* and precise value of the Ge content, *as seen by MAD*, from DAFS spectra. Then, for each of them, a cusp best fit was obtained over the entire energy range by fitting Eq. (5) to the data and refining $\frac{|F_{Ge}|}{|F_{Si}|}$ and $\varphi_{Si} - \varphi_{Ge}$.

Due to the grazing incidence/outgoing geometry the Distorted Wave Born Approximation must be considered for writing the structure factor and further analysing DAFS data (see for instance references [31,75,80]). It is worth noting that Eqs. (2), (4) and (5) still hold since for large (in-plane) scattering angles (2θ), as is the case in this experiment, the total intensity is the product of the modulus squared of the structure factor calculated in the Born Approximation times a DWBA pre-factor [75,80]. Provided that the substrate does not contain resonant atoms (Ge atoms), the intensity pre-factor (including the reflection coefficient at the Si surface) has no anomalous energy dependence at the edge. We also want to note that something like a GeSi wetting layer could exist on the top of the Si substrate (see for instance [81]) that could introduce anomalous variations of the DWBA pre-factor. In the case of this sample, when including a wetting layer in our simulations no noticeable change is observed

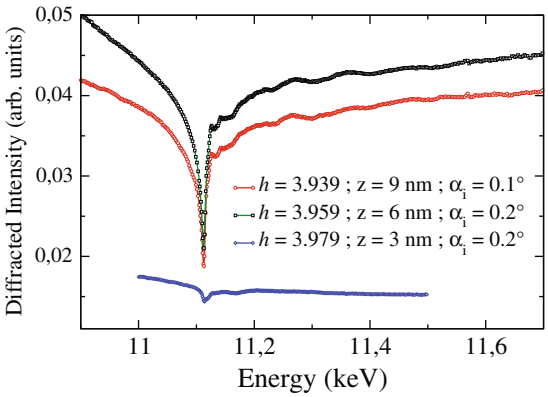

Fig. 10. GIDAFS spectra measured at fixed $\boldsymbol{Q}(3.939, 0, 0)$, $\boldsymbol{Q}(3.959, 0, 0)$ and $\boldsymbol{Q}(3.979, 3.979, 0)$ vectors to which correspond iso-strain regions at different heights z in the dome.

Table 1. Ge content x_{Ge} and the crystallographic phase difference $\varphi_{Si} - \varphi_{Ge}$ obtained by fitting Eq. (4) to GIDAFS spectra (see Sect. 3.1). z is the height above the Si substrate surface of the iso strain region inside the dome selected by the diffraction condition. $\Delta\psi = \varphi_0 - \varphi_{Ge} - \frac{\pi}{2}$ (rad.) and S_D are the Extended DAFS scale factor and crystallographic phase correction, respectively. Their values are calculated with $\varphi_T - \varphi_{Ge}$ and β_{TGe} (Eqs. (9), (10) and (11)).

h,k,l	x_{Ge}	x_{Ge} ZB	$\varphi_{Si} - \varphi_{Ge}$ (rad.)	z (nm)	α_i (°)	$\Delta\psi$ (rad.)	S_D
3.939,0,0	0.58±.02	0.67±.02	-0.9	9.1	.1	-2.2	3.2
3.959,0,0	0.66±.02	0.80±.02	-1.0	6.0	.2	-1.55	3.0
3.972,3.972,0	0.24±.02	0.26±.02	-0.5	4.0	.2	-1.8	4.6
3.974,3.974,0	0.16±.02	0.16±.02	-0.6	3.7	.2	-2.0	6.6
3.979,3.979,0	0.09±.02	0.09±.02	-0.8	3.0	.2	-2.2	-

in comparison with the one of the wetting layer-free {dome+substrate} scattered intensity.

Then, for each DAFS spectrum, the Ge content is obtained in a straightforward way by using the following formula: $\frac{|F_{Ge}|}{|F_{Si}|} \approx \frac{x_{Ge} f^0_{Ge}}{(1-x_{Ge}) f^0_{Si}}$, where x_{Ge} is the Ge concentration. Table 1 reports x_{Ge} calculated for the different $\boldsymbol{Q}(h, k, l)$ vectors. The values are in very good agreement with those obtained from the simulated MAD (see Fig. 9). The table also gives the EDAFS normalisation factor, S_D, and the EDAFS crystallographic phase correction, $\varphi_0 - \varphi_{Ge}$, calculated with the fit parameters $\frac{|F_{Ge}|}{|F_{Si}|}$ and $\varphi_{Si} - \varphi_{Ge}$ (Eqs. (9) and (10)). Interestingly, Table 1 shows that $\varphi_{Si} - \varphi_{Ge}$ is never equal to zero and always negative. It can be as high as -1 rad. A negative value means that the intensity level after the edge is being lowered. This means that diffraction does not "see" a homogeneous GeSi alloy in the iso strain region selected by diffraction. There could be several reasons for retrieving non zero, negative $\varphi_{Si} - \varphi_{Ge}$: e.g. the spatial distributions of Si and Ge atoms are not equivalent. This is the case for h close to 4 since part of the strained Si substrate underneath the dome contributes to the signal. For this h value indeed, our simulations give a negative phase difference of about the right value. Instead, for h as low as h=3.939 and h=3.959, simulations with a homogeneous Ge and Si spatial distributions do not explain the negative values. While there is still work to be done to understand that point, a relevant question is:

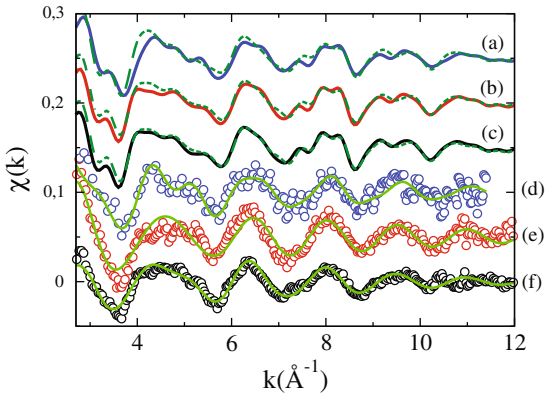

Fig. 11. GI-EDAFS spectra (open circles) measured at fixed vectors (d) $\boldsymbol{Q}(3.974, 3.974, 0.0)$, (e) $\boldsymbol{Q}(3.959, 0, 0.0)$ and (f) $\boldsymbol{Q}(3.939, 0, 0.0)$, to which correspond iso-strain regions of different heights z in the dome, together with the best fit curves (solid lines). The fitting was performed in k-space in the range of 3 to 10 Å^{-1}. Experimental data are also compared to EDAFS oscillations (a,b,c) calculated at the same $\boldsymbol{Q}$ vectors as (d,e,f) using the model cluster (solid lines). Broken lines show EDAFS oscillations calculated for the relaxed alloys with 0.6 (b,c) and 0.5 (a) Ge contents to compare the effect of strain and composition.

what would the Ge content be if one assumes a homogeneous GeSi alloy to fit the DAFS spectrum ? To answer this question, we have fitted the DAFS cusp with a Ge_xSi_{1-x} alloy and a Zinc-Blende structure ($\varphi_{Si} - \varphi_{Ge} = 0$). The fit was done in the energy range below the edge (in the region where the exact value of $\varphi_{Si} - \varphi_{Ge}$ has little influence). The results are given in Table 1 (x_{Ge} (ZB)). They show that the Ge content is the same as the one found with MAD approach for $\varphi_{Si} - \varphi_{Ge}$ values higher than -0.8 rad. For $\varphi_{Si} - \varphi_{Ge} = -0.9$ rad the difference is about 10%.

The EDAFS oscillations, extracted by spline subtraction of the smooth atomic background are shown in Fig. 11 as a function of the wavenumber k, and labeled by the corresponding h value. A quantitative analysis of EDAFS oscillations allows a direct determination of the Ge coordination numbers (local composition) and Ge-Ge(Si) interatomic distances (strain) in the iso strain region selected by the diffraction condition. To do so, we fitted the parametric expression for $\chi_Q(k)$ (Eq. (17)) to the experimental EDAFS oscillations.

The analysis was performed according to the standard EXAFS formalism. Theoretical phases and amplitudes were generated by the *Feff8.02* code [82], by using potential self-consistency and taking into account the [001] polarization direction of the incident and outgoing X-ray photons. A cluster of 0.6 nm was generated with a central Ge absorber surrounded either by Ge or Si backscatterer atoms. The fitting of theory to experiment was performed by the least-squares minimization code *Ifeffit* implemented in the Artemis package [83,84]. The presence of Si in the Ge environment is simulated by splitting the relevant scattering paths into Ge-Ge and Ge-Si pairs and combining the corresponding theoretical signals while keeping the overall coordination fixed to the zincblende values ($N = N_{Ge} + N_{Si} = 4$, for first coordination shell and $N = N_{Ge} + N_{Si} = 12$, for second one). Triangular multiple scattering (MS) paths Ge-Ge(Si)-Ge(Si) were also included when relevant. The best fit curves are shown in Fig. 11, as solid curves, and best fit parameters in Table 2.

A small change in shape, a bump, is observed for $h = 3.974$ at about 4.2 Å^{-1}, which is well reproduced by the fit. It is due to a slight change both in coordination numbers and interatomic distances. The oscillations profile at low k is very sensitive to the presence of Si as a scatterer, due to different backscattering amplitude functions

Table 2. Best fit results for interatomic distances (R in Å), Ge concentration for first (I) (x_{Ge}) and second (II) (y_{Ge}) coordination shells. Errors on distances are ±0.02 and ±0.03 Å for first and second shell, respectively. Errors on concentration are about ±0.1. Interatomic distances for bulk Ge, Si and $Ge_{0.5}Si_{0.5}$ relaxed alloy are given for comparison.

Sample	h k l	x_{Ge}	y_{Ge}	$R(GeGe(SiSi))_I$	$R(GeSi)_I$	$R(GeGe(SiSi))_{II}$	$R(GeSi)_{II}$
Bulk Ge(Si)	-	1	1	2.45(2.35)	-	4.0(3.83)	-
$Ge_{0.5}Si_{0.5}$	-	0.5	0.5	2.43	2.40	3.93	3.92
Experiment	3.974 3.974 0	0.6	0.4	2.40	2.40	3.9	3.9
	3.959 0 0	0.6	-	2.40	2.39	3.9	3.9
	3.939 0 0	0.7	-	2.42	2.40	3.9	3.9

of Ge and Si. In Table 2, the values of the interatomic distances are compared with those of bulk Ge and Si and with those of relaxed $Ge_{0.5}Si_{0.5}$ alloy. For comparison, Fig. 11 also shows the $\chi(k)$ oscillations calculated by the atomistic model and Eq. (8) (Eq. (17) can also be used). We observe a tendency of increasing values of both Ge-Ge and Ge-Si interatomic distances while going from the base to the top of the dome, in agreement with lattice relaxation, and a slight increase of Ge concentration along the growth direction, z. Nevertheless, regarding strain, a better signal-to-noise ratio and measurements with polarization both parallel and perpendicular to the surface would be needed to provide a more precise determination of interatomic distances. Regarding composition, the Ge concentration values have been split out, for $h = 3.974$, in x_{Ge} and y_{Ge}, corresponding to the Ge population of first (I) and second (II) shell respectively, and both refined as fit parameters. They should be equal for a random alloy and they are meaningful to detect possible deviations due to the asymmetry of composition at dome/substrate interface. Indeed, in this case the region probed by EDAFS is a thin slice at the very base of the dome (see Fig. 3), so that the weight of the interface in the EDAFS signal is enhanced with respect to the upper regions. The introduction of this extra parameter improved the fit quality only for the spectrum corresponding to $h = 3.974$. If we consider that x_{Ge} is closer to the real average composition, we can state that dome composition, even at its base is at least $Ge_{0.6}Si_{0.4}$. This is in contrast with the value of about 20% Ge found by MAD for the same z value. For $h = 3.939$ and $h = 3.959$, the fit was not improved by splitting out the Ge content and we report a single x_{Ge} value in Table 2. We also observe a slight increase of Ge content from the base to the top of the dome. Regarding the interface nature, one can compare our results with the findings reported in references [71,85] for domes grown at 720–740 °C: after a selective chemical etching of the domes the substrate underneath has a tree-stump shaped structure. The interface dome/substrate is at the strained Si stump, the height of which is of about 2 nm. The composition profile is rather abrupt, switching from the almost pure Si in the stump to the about constant 30% Ge concentration in the dome. This is in good agreement with our results, considering that in our case the higher Ge content is due to the lower growth temperature of 650 °C. In the present study the stump/dome interface is located, according to Fig. 9 at $h = 3.98$ ($z = 2.1$ nm, the zero of our z-scale correspond to the flat bulk Si substrate and $h = 4$). The relevance of EDAFS results resides in the direct determination of dome composition given by an EXAFS-like short-range-order probe. It is affected by errors due to signal to noise but it is free from spurious effects that can be present in MAD extraction due to the proximity of the Si substrate's diffraction peak.

5.2 AlGaN nanowires

III-Nitride semiconductor materials are of major importance for blue and UV light emission applications, although their ultimate potentialities are still plagued by the

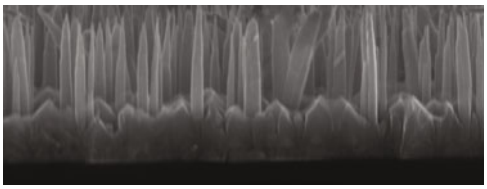

Fig. 12. Scanning Electron Microscopy of AlGaN nanowires grown on Si(111) [94].

high density of dislocations (10^7–10^{10} cm^{-2}) and other structural defects resulting from the lack of lattice-adapted substrates. By contrast, GaN nanowires (NWs) exhibit an exceptional crystalline quality [86,87], which makes them serious candidates for the design of high efficiency III-N NWs-based devices. Actually, it has already been demonstrated that GaN/InGaN/GaN and AlGaN/GaN/AlGaN NW heterostructures can be succesfully grown to achieve light emitting diodes (LEDs) in the visible [88,89] and UV [90] range, respectively.

It has been established that GaN NW growth is mostly driven by in-plane Ga diffusion towards NW base, followed by a diffusion on their side and, finally, incorporation on top, provided that the growth temperature is high enough [91–94]. As surface adatom diffusion in the basal plane as well as along the $(1\bar{1}00)$ walls of NWs [94–96] is critical, it is expected that growth of ternary (InGaN or AlGaN) NWs will be strongly dependent on the difference in diffusion of different adatom species. In particular, in the case of AlGaN NWs, the question arises of predicting/controlling their composition, due to the fast diffusion of Ga compared to Al. It is the goal of this study to provide insight on the growth mechanism of AlGaN NWs and in particular to clarify the issue of a possible composition gradient related to the different diffusion lengths of Al and Ga adatoms.

5.2.1 Samples

The sample (Fig. 12) was grown by Plasma-Assisted Molecular Beam Epitaxy (PAMBE), catalyst-free, in standard nitrogen-rich conditions. The nominal Al content in the fluxes was 40%. A 3-4 nm AlN buffer layer was deposited onto the substrate to improve wire orientation [91,94]. Figure 12 shows 0.7 μm long AlGaN nanowires whose base is embedded in a rough 300 nm thick AlGaN layer. The question is twofold: what is the Al content in the wires and is there any Al/Ga concentration gradient?

5.2.2 Multiwavelength anomalous diffraction

MAD and DAFS measurements were performed at beamline BM2 at the ESRF. A linear gas-detector (Vantec^{TM}, Bruker) was used to record the scattered intensity. MAD 2D maps were measured at 12 energies across the Ga K-edge (10367 eV), close to the specular GaN 105 and AlN 105 Bragg reflections. The x-ray beam linear polarisation was perpendicular to the diffraction vector and was oriented 65° with respect to the [0001] direction. The modulus of anomalous (resp. non anomalous) structure factors $|F_{Ga}|$ (resp. $|F_{Al+N}|$) and the phase difference $\varphi_{Al+N} - \varphi_{Ga}$ were recovered as a function of the reciprocal lattice unit h,l by *NanoMAD* [44] ($F_{Ga,Al+N}(hkl) = |F_{Ga,Al+N}(hkl)|\, e^{i\varphi_{Ga,Al+N}(hkl)}$).

Figure 13 shows 2D maps in reciprocal space representing the modulus of anomalous and non anomalous structure factors. It also shows the positions of relaxed GaN and AlN 105 reflections. At first glance, there are two scattering spots, one centered

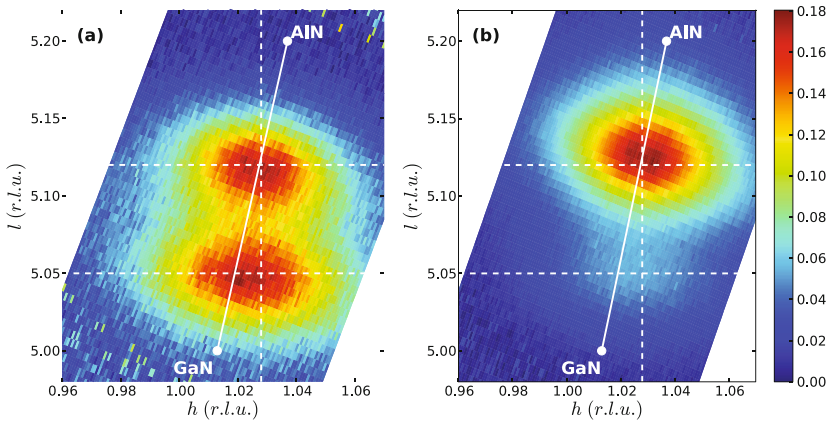

Fig. 13. 2D experimental map recorded around the 105 reflection for AlGaN nanowires, extracted using MAD: (a) Ga (F_{Ga}) and (b) Al and N ($F_{Al} + F_N$) partial structure factors. The two main scattering spots correspond to Ga-rich and Al-rich AlGaN contributions, between the positions for bulk AlN and GaN (indicated by white dots). The cross points of dash-lines correspond to the reciprocal space points where the DAFS spectra were measured.

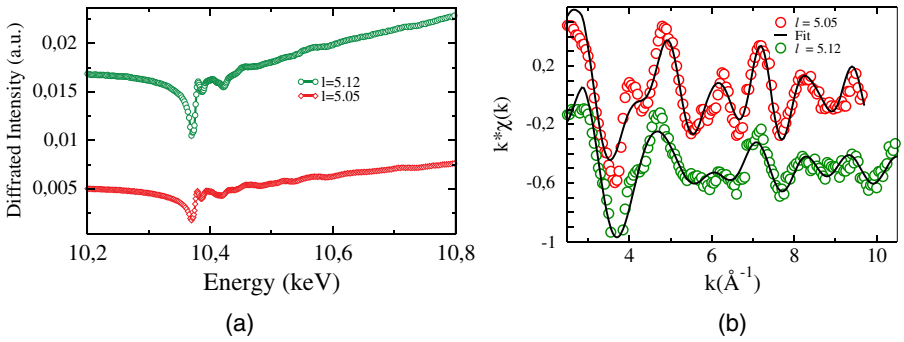

Fig. 14. (a) DAFS spectra (corrected for fluorescence) measured at $h = 1.03$, $l = 5.12$ and $h = 1.03$, $l = 5.05$ ($k = 0$), see figure 13. (b) Ga K-edge EDAFS oscillations for GaAlN nanowires at $h = 1.03$, $l = 5.12$ and $h = 1.03$, $l = 5.05$ ($k = 0$), together with the corresponding best fit curves.

at $h = 1.02$, $l = 5.05$ and the other, centered at $h = 1.03$, $l = 5.12$, i.e. very close to the relaxed AlGaN line, which connects the relaxed GaN and AlN 105 reflections. The former corresponds to a Ga rich AlGaN whereas the latter corresponds to an Al rich AlGaN. To obtain the Al content, DAFS spectra were measured at these two positions ($h = 1.03$, $l = 5.05$ and $h = 1.03$, $l = 5.12$).

Figure 14 shows the intensity variation as a function of the energy, measured by the linear detector. Fitting of DAFS cusps, assuming an AlGaN compounds with the wurzite structure, gives an Al content of 0.7 (resp. 0.11) for $h = 1.03$, $l = 5.12$ (resp. $h = 1.03$, $l = 5.05$). An Al content of 0.11 is consistent with the cathodoluminescence of the wires, therefore we have safely attributed the scattered intensity at $h = 1.03$, $l = 5.05$ to the wires. A close inspection of Fig. 13 shows that the Ga and the Al + N structure factors of the Al rich spot are not superposed, as highlighted by the horizontal dotted lines. This means that a composition gradient/segregation exists in the 2D AlGaN layer which grows between the wires.

Table 3. EDAFS best fit results for nanowires. Error bars on interatomic distances range from ± 0.01 to 0.03 Å. Debye-Waller values range from 3 to 7 10^{-3}Å^2. Error bars on x_{Al} are about 0.05. Labels ⊥ and // respectively correspond to directions perpendicular and parallel to the substrate surface.

Sample	Bulk GaN	Bulk AlN	nanowires l=5.05	nanowires l=5.12
R(Ga-N) (Å)	1.947	-	1.94	1.93
$R(Ga-Ga)_{\perp}$ (Å)	-	-	3.15	3.13
$R(Ga-Ga)_{//}$ (Å)	3.189	-	3.17	3.14
$R(Ga-Al)_{\perp}$ (Å)	-	3.11	3.12(fixed)	3.12
$R(Ga-Al)_{//}$ (Å)	-	-	3.12(fixed)	3.12
c (Å)	5.186	4.982	5.18	5.10
x_{Al}	0	1	0.1	0.45
c/a	1.626	1.6	1.64	1.62

5.2.3 Diffraction anomalous fine structure

Figure 14 shows the background subtracted EDAFS oscillations together with the corresponding best fit curves. Best fit results are summarized in Table 3. The difference between the two spectra is quite remarkable, both in the raw χ(k) and FT spectra. It is due to the change in the local Ga environment related to the change in composition of the two different regions of the nanocolumn selected by diffraction. The sample is much more Al- rich at $l = 5.12$. Quantitative results have been obtained by least square fitting of raw χ(k) using *Ifeffit* code implemented in the Artemis package. Theoretical phases and amplitudes were generated using the *Feff8.2* software. DAFS corrections to phases and amplitudes have been applied according to a first order χ approximation analysis scheme as described in reference [16]. They are deduced by fitting the smooth part of the DAFS spectrum. Polarization of the X-ray beam has been taken into account considering that in the experimental diffraction conditions the vector was not very far from being parallel to the sample surface (about 20°). Fits have been performed imposing hexagonal symmetry and taking into account single and multiple (three atoms) scattering paths up to a distance of about 4.5 Åfrom the central Ga absorber.

Interatomic distances are coherent with composition although the c/a ratio shows that the strain is not completely relaxed (Table 3). The Al content varies from $x = 0.1$ at $l = 5.05$ to $x = 0.45$ at $l = 5.12$. It is worth noting that Al contents as determined by MAD and EDAFS in the Ga rich region ($l = 5.05$) are identical. Both probes see an homogeneous alloy (NWs). On the contrary, a significant difference is found for the Al content of the Al-rich region, with respect to the value found by fitting DAFS cusp, $x = 0.70$ and $x = 0.45$, respectively. This is coherent with the presence of an Al gradient/segregation as suggested by the comparison of the anomalous 2D maps of Fig. 13. DAFS and EDAFS can probe, in case of an interface region as shown in Sect. 5.1, or of gradient, clustering and in general structural inhomogeneities, different regions of the sample in real space.

In the present case, it is interesting to note that the bottom of the GaN NWs is embedded in the 2D AlGaN layer and consequently compressed in the longitudinal direction. So, both the GaN NWs and the 2D AlGaN layer are somehow matched along the [0001] direction. Then, X-ray diffraction probes, by the 105 reflection, both the NWs and the AlGaN layer, the Al content as determined by MAD corresponds to the composition average. By comparison, EDAFS oscillations at the Ga K-edge probe mainly the Ga rich NWs giving lower value of the Al content. This means

that the comparison of EDAFS and DAFS/MAD results can be crucial for a correct determination of the actual composition.

6 Conclusion and perspectives

In this paper we have given a thorough review of the application of MAD and DAFS to the study of semiconductor nanostructures. With the aim to introduce the reader to a technique that is still under-exploited, we have given:

- the basic principle of MAD and DAFS
- a thorough description of data reduction and analysis
- a selection of a few but meaningful examples.

A particular attention has been given to MAD/GIMAD that is now routinely used for the analysis of epitaxial nano-structures. It has a number of remarkable features compared to standard X-ray diffraction (including Grazing Incidence Diffraction):

- it allows the determination of the chemical composition in different regions of the sample (iso-strain approach), and the data acquisition is quite fast: e.g. from a few minutes up to 1 hour for 12-energies measurements involving a single scan in reciprocal space, for a few monolayers of material.
- it can be combined with a 1D or 2D detector for faster measurements
- the speed of the measurements allows in-situ analysis [50,97,98]
- analysis is straightforward and does not generally require a structural model.

The most important limit of MAD/GIMAD is that this technique can not separate the signal from the nano-objects and the diffraction tails of the substrate, or between different iso-strain regions with the same strain (e.g. when studying buried objects or materials separated by a coherent interface). Most often, this separation can be performed using the GIDAFS technique.

On the experimental side, new technical/instrumental improvements are foreseen:

- X-ray detectors play a key role in the overall performance of synchrotron-based experimental setups. 2D pixel detectors are particularly attractive to achieve precise measurements with a very high dynamical range (diffraction measurement for instance), and to avoid wasting a very significant part of the incoming photon flux by inserting attenuators. The use of 2D pixel detectors speeds up reciprocal space maps acquisition and consequently MAD and DAFS measurements by allowing the simultaneous acquisition of several DAFS and fluorescence spectra. This will definitely open the route for a better understanding and control of structural and chemical changes under controlled atmosphere, as a function of annealing parameters (T, atmosphere). This kind of detector will also speed up DAFS studies of powder nanostructures [99].
- For grazing incidence MAD and DAFS experiments, another major improvement will be to stabilize the optical beam geometry and to focus the beam on the sample. This can be achieved with achromatic Kirkpatrick-Baez focusing mirrors [100], which allow to focus the beam with a spot size smaller than 1 square micron, and therefore to increase the incoming intensity caught by the sample. This will help to avoid DAFS spectra distortions induced by the beam geometrical changes as a function of energy. Furthermore, the use of focused X-ray beams gives the opportunity to provide structural and chemical information with a spatial resolution given by the spot size. This will allow to perform MAD and DAFS studies at this scale, a great opportunity in the study of heterogeneous samples.

– Regarding synchrotron sources, new beamlines will be available, as for example the new SIRIUS beamline at synchrotron SOLEIL (St Aubin, France). It is partially dedicated to DAFS and GIDAFS in the intermediate energy range (2–10 keV). This gives new possibilities, for instance, In L-edge can be reached allowing a direct In site study in In-based nanostructures. In addition, beamline BM2 of ESRF, where most of the work shown in this paper has been carried out, is now being fully upgraded. The new optics and monochromator have been designed taking into account DAFS experimental requirements and its performances for this kind of experiments will be strongly improved.

On the materials side, the work achieved so far is small compared to the large diversity of nanostructured semiconductors. One deals with continuously evolving materials which have almost immediate technological applications. For example, ternary InGaN NWs with a spontaneous core-shell structure [51] or AlGaN NWs are under study to solve the issue of composition, strain, local order, to provide a feedback to the spontaneous core shell growth and to explain their optical properties. The effect of high temperature annealing is also being studied on QDs superlattices of GaN/AlGaN, or ternary AlGaN thin films to relate structural change/phase separation to optical properties.

We acknowledge the French CRG at the ESRF for granting beam time and support to developing DAFS spectroscopy at the beamlines BM2 and BM32. We are very grateful to J.F. Bérar, S. Arnaud, B. Caillot and N. Boudet for their constant help to the development of DAFS spectroscopy at BM2. We thank the ESRF for allocating beamtime and ID1 and ID3 staff (T. Metzger, B. Krause, D. Vermeille, R. Felici) for help with the experiments. We are very grateful to S. Grenier and A. Letoublon who were the first PhD student and Post-doctoral fellow to develop GIDAFS spectroscopy and applied it to nanostructures, and J. Coraux for further advancing this method. The authors are indebted to O. Landré, G. Tourbot, B. Daudin, Z. Zhang, G. Bauer who have shown interest in MAD and DAFS, grew the samples and shared their deep knowledge on the materials. MGP and NAK acknowledge support of Spanish Ministry of Science and Education project MAT2008-03074.

References

1. R. Kahn, R. Fourme, R. Bosshard, M. Chiadmi, J. Risler, O. Dideberg, J. Wery, FEBS Lett. **179**, 133 (1985), ISSN: 0014-5793
2. W. Hendrickson, Science **254**, 51 (1991)
3. J. Hodeau, V. Favre-Nicolin, S. Bos, H. Renevier, E. Lorenzo, J. Berar, Chem. Rev. **101**, 1843 (2001)
4. H. Stragier, J. Cross, J. Rehr, L. Sorensen, C. Bouldin, J. Woicik, Phys. Rev. Lett. **69**, 3064 (1992), ISSN: 0031-9007
5. H. Renevier, J. Hodeau, P. Wolfers, S. Andrieu, J. Weigelt, R. Frahm, Phys. Rev. Lett. **78**, 2775 (1997), ISSN: 0031-9007
6. Y. Murakami, H. Kawada, H. Kawata, M. Tanaka, T. Arima, Y. Moritomo, Y. Tokura, Phys. Rev. Lett. **80**, 1932 (1998)
7. J. García, G. Subías, M. Proietti, H. Renevier, Y. Joly, J. Hodeau, J. Blasco, M. Sánchez, J. Bérar, Phys. Rev. Lett. **85**, 578 (2000), ISSN: 0031-9007
8. Y. Cauchois, C. Bonnelle, Comptes Rendus de l'Académie des Sciences **242**, 1596 (1956)
9. Y. Cauchois, Comptes Rendus de l'Académie des Sciences **242**, 100 (1956)
10. T. Fukamachi, S. Hosoya, T. Kawamura, J. Hastings, J. Appl. Crystallography **10**, 321 (1977), ISSN: 0021-8898
11. U.W. Arndt, T.J. Greenhough, J.R. Helliwell, J.A.K. Howard, S.A. Rule, A.W. Thompson, Nature **298**, 835 (1982), ISSN: 0028-0836

12. I. Arčon, A. Kodre, D. Glavič, M. Hribar, Le Journal de Physique Colloques **48**, C9 (1987)
13. I.J. Pickering, M. Sansone, J. Marsch, G.N. George, Japanese J. Applied Physics **32 Suppl2**, 206 (1993)
14. I.J. Pickering, M. Sansone, J. Marsch, G.N. George, J. American Chemical Society **115**, 6302 (1993)
15. L. Sorensen, J. Cross, M. Newville, B. Ravel, J.J. Rehr, H. Stragier, C. Bouldin, J. Woicik, in *ResonantAnomalous X-Ray Scattering: Theory and Applications*, edited by G. Materlik, J. Sparks, K. Fischer (Elsevier Science edn., Amsterdam, 1994)
16. M. Proietti, H. Renevier, J. Hodeau, J. García, J. Bérar, P. Wolfers, Physical Review B **59**, 5479 (1999), ISSN: 0163-1829
17. Y. Joly, Phys. Rev. B **63**, 125120 (2001), ISSN: 1098-0121
18. D.C. Meyer, A. Kupsch, P. Paufler, J. Synchrotron Radiation **10**, 144 (2003), ISSN: 09090495
19. H. Renevier, S. Grenier, S. Arnaud, J.F. Bérar, B. Caillot, J.L. Hodeau, A. Letoublon, M.G. Proietti, B. Ravel, J. Synchrotron Radiation **10**, 435 (2003), ISSN: 0909-0495
20. J. Woicik, J. Cross, C. Bouldin, B. Ravel, J. Pellegrino, B. Steiner, S. Bompadre, L. Sorensen, K. Miyano, J. Kirkland, Phys. Rev. B **58**, R4215 (1998), ISSN: 0163-1829
21. D. Meyer, K. Richter, P. Paufler, G. Wagner, Phys. Rev. B **59**, 15253 (1999), ISSN: 0163-1829
22. T. Bigault, F. Bocquet, S. Labat, O. Thomas, H. Renevier, Phys. Rev. B **64** (2001), ISSN: 0163-1829
23. G. Luo, Z. Mai, T. Hase, B. Fulthorpe, B. Tanner, C. Marrows, B. Hickey, Phys. Rev. B **64**, 245404 (2001), ISSN: 0163-1829
24. H.H. Lee, M.S. Yi, H.W. Jang, Y. Moon, S. Park, D.Y. Noh, M. Tang, K.S. Liang, Appl. Phys. Lett. **81**, 5120 (2002), ISSN: 00036951
25. O. Ersen, V. Pierron-Bohnes, M. Tuilier, C. Pirri, L. Khouchaf, M. Gailhanou, Phys. Rev. B **67**, 94116 (2003), ISSN: 0163-1829
26. S. Grenier, M.G. Proietti, H. Renevier, L. Gonzalez, J.M. García, J.M. Gérard, J. García, J. Synchrotron Radiation **8**, 536 (2001), ISSN: 09090495
27. S. Grenier, M.G. Proietti, H. Renevier, L. González, J.M. García, J. García, Europhysics Letters (EPL) **57**, 499 (2002), ISSN: 0295-5075
28. A. Letoublon, V. Favre-Nicolin, H. Renevier, M.G. Proietti, C. Monat, M. Gendry, O. Marty, C. Priester, Phys. Rev. lett. **92**, 186101 (2004), ISSN: 1079-7114
29. J. Coraux, M.G. Proietti, V. Favre-Nicolin, H. Renevier, B. Daudin, Phys. Rev. B **73**, 205343 (2006)
30. J. Coraux, V. Favre-Nicolin, M.G. Proietti, B. Daudin, H. Renevier, Phys. Rev. B **75**, 235312 (2007)
31. U. Pietsch, V. Holý, T. Baumbach, *High-Resolution X-Ray Scattering: From Thin Films to Lateral Nanostructures*, 2nd edn. (Springer-Verlag, New York Inc., 2004), ISBN: 0387400923
32. J. Stangl, V. Holý, G. Bauer, Reviews of Modern Physics **76**, 725 (2004)
33. I. Kegel, T.H. Metzger, A. Lorke, J. Peisl, J. Stangl, G. Bauer, J.M. García, P.M. Petroff, Phys. Rev. Lett. **85**, 1694 (2000)
34. G. Williams, M. Pfeifer, I. Vartanyants, I. Robinson, Phys. Rev. B **73** (2006), ISSN: 1098-0121
35. S. Grenier, Ph.D. thesis, Université Joseph Fourier, Grenoble, France, 2001
36. J. Coraux, Ph.D. thesis, Université Joseph Fourier, 2006
37. D.H. Templeton, L.K. Templeton, J.C. Phillips, K.O. Hodgson, Acta Crystallographica Section A **36**, 436 (1980), ISSN: 0567-7394
38. E.N. Ovchinnikova, V.E. Dmitrienko, Acta Crystallographica Section A Foundations of Crystallography **53**, 388 (1997), ISSN: 0108-7673
39. E.N. Ovchinnikova, V.E. Dmitrienko, Acta Crystallographica Section A Foundations of Crystallography **56**, 2 (2000), ISSN: 0108-7673
40. V.E. Dmitrienko, K. Ishida, A. Kirfel, E.N. Ovchinnikova, Acta Crystallographica Section A Foundations of Crystallography **61**, 481 (2005), ISSN: 0108-7673

41. R. Magalh aes-Paniago, G. Medeiros-Ribeiro, A. Malachias, S. Kycia, T.I. Kamins, R.S. Williams, Phys. Rev. B **66**, 245312 (2002)
42. A. Malachias, S. Kycia, G. Medeiros-Ribeiro, R. Magalh aes-Paniago, T.I. Kamins, R.S. Williams, Phys. Rev. Lett. **91**, 176101 (2003)
43. T.U. Schülli, J. Stangl, Z. Zhong, R.T. Lechner, M. Sztucki, T.H. Metzger, G. Bauer, Phys. Rev. Lett. **90**, 066105 (2003)
44. V. Favre-Nicolin, *NanoMAD* (2011)
45. H. Dosch, *Critical Phenomena at Surfaces and Interfaces* (Springer Verlag, New York, 1992), ISBN: 0367-0325
46. L.N. Coelho, R. Magalh aes-Paniago, A. Malachias, J.G. Zelcovit, M.A. Cotta, Appl. Phys. Lett. **92**, 021903 (2008), ISSN: 00036951
47. N.A. Katcho, M. Richard, M.G. Proietti, H. Renevier, C. Leclere, V. Favre-Nicolin, J.J. Zhang, G. Bauer, Europhys. Lett. **93**, 66004 (2011), ISSN: 0295-5075
48. J. Cross, M. Newville, J. Rehr, L. Sorensen, C. Bouldin, G. Watson, T. Gouder, G. Lander, M. Bell, Phys. Rev. B **58**, 11215 (1998), ISSN: 0163-1829
49. H. Stragier, Ph.D. thesis, University of Washington, 1993
50. J. Coraux, H. Renevier, M.G. Proietti, V. Favre-Nicolin, B. Daudin, G. Renaud, Physica Status Solidi (b) **243**, 1519 (2006)
51. K. Hestroffer, R. Mata, D. Camacho, C. Leclere, G. Tourbot, Y.M. Niquet, A. Cros, C. Bougerol, H. Renevier, B. Daudin, Nanotechnology **21**, 415702 (2010), ISSN: 0957-4484
52. V.E. Dmitrienko, Acta Crystallographica Section A Foundations of Crystallography **39**, 29 (1983), ISSN: 0108-7673
53. F. d'Acapito, F. Boscherini, S. Mobilio, A. Rizzi, R. Lantier, Phys. Rev. B **66**, 205411 (2002), ISSN: 0163-1829
54. D.T. Cromer, D.A. Liberman, J. Chem. Phys. **53**, 1891 (1970), ISSN: 00219606
55. J. Als-Nielsen, D. McMorrow, *Elements of Modern X-ray Physics*, 1st edn. (John Wiley & Sons, 2001), ISBN: 0471498572
56. J. Toll, Phys. Rev. **104**, 1760 (1956), ISSN: 0031-899X
57. J.M. Bijvoet, A.F. Peerdeman, A.J. van Bommel, Nature **168**, 271 (1951), ISSN: 0028-0836
58. K. Hestroffer, C. Leclere, C. Bougerol, H. Renevier, B. Daudin, Phys. Rev. B **84**, 245302 (2011)
59. M. Richard, V. Favre-Nicolin, G. Renaud, T.U. Schulli, C. Priester, Z. Zhong, T. Metzger, Appl. Phys. Lett. **94**, 013112 (2009)
60. A. Rastelli, M. Stoffel, J. Tersoff, G.S. Kar, O.G. Schmidt, Phys. Rev. Lett. **95**, 026103 (2005)
61. M. Richard, Ph.D. thesis, Université Grenoble I, 2007
62. N. Gogneau, D. Jalabert, E. Monroy, T. Shibata, M. Tanaka, B. Daudin, J. Appl. Phys. **94**, 2254 (2003), ISSN: 10897550
63. V. Chamard, T.H. Metzger, M. Sztucki, V. Holý, M. Tolan, E. Bellet-Amalric, C. Adelmann, B. Daudin, H. Mariette, Europhys. Lett. **63**, 268 (2003), ISSN: 0295-5075, 1286-4854
64. O.G. Schmidt, K. Eberl, IEEE Transactions on Electron Devices **48**, 1175 (2001), ISSN: 0018-9383
65. G.S. Kar, S. Kiravittaya, U. Denker, B. Nguyen, O.G. Schmidt, Appl. Phys. Lett. **88**, 253108 (2006), ISSN: 00036951
66. L.A. Montoro, M.S. Leite, D. Biggemann, F.G. Peternella, K.J. Batenburg, G. Medeiros-Ribeiro, A.J. Ramirez, J. Phys. Chem. C **113**, 9018 (2009)
67. X. Liao, J. Zou, D. Cockayne, J. Wan, Z. Jiang, G. Jin, K. Wang, Phys. Rev. B **65**, 153306 (2002), ISSN: 0163-1829
68. F. Boscherini, G. Capellini, L. Di Gaspare, F. Rosei, N. Motta, S. Mobilio, Appl. Phys. Lett. **76**, 682 (2000), ISSN: 00036951
69. T. Schülli, G. Vastola, M. Richard, A. Malachias, G. Renaud, F. Uhlík, F. Montalenti, G. Chen, L. Miglio, F. Schäffler, et al., Phys. Rev. Lett. **102**, 25502 (2009), ISSN: 0031-9007

70. M. Leite, A. Malachias, S. Kycia, T. Kamins, R. Williams, G. Medeiros-Ribeiro, Phys. Rev. Lett. **100**, 226101 (2008), ISSN: 0031-9007
71. A. Rastelli, M. Stoffel, A. Malachias, T. Merdzhanova, G. Katsaros, K. Kern, T.H. Metzger, O.G. Schmidt, Nano Letters **8**, 1404 (2008), ISSN: 1530-6984
72. T. Schülli, M. Stoffel, A. Hesse, J. Stangl, R. Lechner, E. Wintersberger, M. Sztucki, T. Metzger, O. Schmidt, G. Bauer, Phys. Rev. B **71**, 35326 (2005), ISSN: 1098-0121
73. G. Katsaros, G. Costantini, M. Stoffel, R. Esteban, A. Bittner, A. Rastelli, U. Denker, O. Schmidt, K. Kern, Phys. Rev. B **72**, 195320 (2005), ISSN: 1098-0121
74. G. Biasiol, S. Heun, Physics Reports **500**, 117 (2011), ISSN: 0370-1573
75. M.G. Proietti, J. Coraux, H. Renevier, in *Characterization of Semiconductor Heterostructures and Nanostructures*, edited by C. Lamberti (Elsevier Science edn., Amsterdam, 2008)
76. S.N. Santalla, C. Kanyinda-Malu, R.M.d.l. Cruz, Nanotechnology **18**, 315705 (2007), ISSN: 0957-4484
77. J. Tersoff, Phys. Rev. B **39**, 5566 (1989)
78. S. Plimpton, J. Computational Physics **117**, 1 (1995), ISSN: 0021-9991
79. S. Plimpton, *LAMMPS molecular dynamics simulator* (1995)
80. I. Kegel, T.H. Metzger, A. Lorke, J. Peisl, J. Stangl, G. Bauer, K. Nordlund, W.V. Schoenfeld, P.M. Petroff, Phys. Rev. B **63**, 035318 (2001)
81. T. Zhou, G. Renaud, C. Revenant, J. Issartel, T.U. Schülli, R. Felici, A. Malachias, Phys. Rev. B **83**, 195426 (2011)
82. A.L. Ankudinov, J.J. Rehr, S.D. Conradson, Phys. Rev. B **58**, 7565 (1998), ISSN: 1098-0121
83. B. Ravel, M. Newville, J. Synchrotron Radiation **12**, 537 (2005), ISSN: 0909-0495
84. M. Newville, J. Synchrotron Radiation **8**, 322 (2001), ISSN: 09090495
85. G. Katsaros, A. Rastelli, M. Stoffel, G. Isella, H.v. Känel, A. Bittner, J. Tersoff, U. Denker, O. Schmidt, G. Costantini, et al., Surface Science **600**, 2608 (2006), ISSN: 0039-6028
86. E. Calleja, M. Sánchez-García, F. Sánchez, F. Calle, F. Naranjo, E. Mu noz, U. Jahn, K. Ploog, Phys. Rev. B **62**, 16826 (2000), ISSN: 0163-1829
87. L. Cerutti, J. Ristić, S. Fernández-Garrido, E. Calleja, A. Trampert, K.H. Ploog, S. Lazic, J.M. Calleja, Appl. Phys. Lett. **88**, 213114 (2006), ISSN: 00036951
88. A. Kikuchi, M. Kawai, M. Tada, K. Kishino, J. Appl. Phys. **43**, L1524 (2004), ISSN: 0021-4922
89. H. Kim, Y. Cho, H. Lee, S.I. Kim, S.R. Ryu, D.Y. Kim, T.W. Kang, K.S. Chung, Nano Letters **4**, 1059 (2004)
90. H. Sekiguchi, K. Kishino, A. Kikuchi, Electronics Lett. **44**, 151 (2008), ISSN: 0013-5194
91. R. Songmuang, O. Landré, B. Daudin, Appl. Phys. Lett. **91**, 251902 (2007), ISSN: 00036951
92. R.K. Debnath, R. Meijers, T. Richter, T. Stoica, R. Calarco, H. Lüth, Appl. Phys. Lett. **90**, 123117 (2007), ISSN: 00036951
93. K. Bertness, A. Roshko, L. Mansfield, T. Harvey, N. Sanford, J. Crystal Growth **310**, 3154 (2008), ISSN: 0022-0248
94. O. Landré, R. Songmuang, J. Renard, E. Bellet-Amalric, H. Renevier, B. Daudin, Appl. Phys. Lett. **93**, 183109 (2008), ISSN: 00036951
95. L. Largeau, D.L. Dheeraj, M. Tchernycheva, G.E. Cirlin, J.C. Harmand, Nanotechnology **19**, 155704 (2008), ISSN: 0957-4484
96. L. Lymperakis, J. Neugebauer, Phys. Rev. B **79**, 241308(R) (2009), ISSN: 1098-0121
97. T.U. Schulli, M. Richard, G. Renaud, V. Favre-Nicolin, E. Wintersberger, G. Bauer, Appl. Phys. Lett. **89**(14), 143114 (2006)
98. M. Richard, T.U. Schulli, G. Renaud, E. Wintersberger, G. Chen, G. Bauer, V. Holy, Phys. Rev. B **80**, 045313 (2009)
99. C. Meneghini, F. Boscherini, L. Pasquini, H. Renevier, J. Appl. Crystallogr. **42**, 642 (2009), ISSN: 0021-8898
100. P. Kirkpatrick, A.V. Baez, J. Optic. Soc. Amer. **38**, 766 (1948)